

Sociohydrodynamics: data-driven modelling of social behavior

Daniel S. Seara,¹ Jonathan Colen,^{1,2,3} Michel Fruchart,^{1,2,4} Yael Avni,¹ David Martin,^{5,6} and Vincenzo Vitelli^{1,2,5}

¹*University of Chicago, James Franck Institute, 929 E 57th Street, Chicago, IL 60637*

²*University of Chicago, Department of Physics, 5720 S Ellis Ave, Chicago, IL 60637*

³*Old Dominion University, Joint Institute on Advanced Computing for Environmental Studies, 1070 University Blvd, Portsmouth, VA, 23703*

⁴*ESPCI, Laboratoire Gulliver, 10 rue Vauquelin, 75231 Paris cedex 05*

⁵*University of Chicago, Kadanoff Center for Theoretical Physics, 933 E 56th St, Chicago, IL 60637*

⁶*University of Chicago, Enrico Fermi Institute, 933 E 56th St, Chicago, IL 60637*

(Dated: January 30, 2024)

Living systems display complex behaviors driven not only by physical forces, but also decision-making guided by information processing and molded by cultural and/or biological evolution. Hydrodynamic theories hold promise for simplified, universal descriptions of these collective behaviors. However, incorporating the individual preferences of decision-making organisms into a hydrodynamic theory is an open problem. Here, we develop a data-driven pipeline that links micromotives to macrobehavior by augmenting hydrodynamics with utility functions that describe individual preferences in microeconomics. We show how to systematically validate the hypotheses underlying this construction from data using statistical tools based on neural networks. We illustrate this pipeline on the case study of human residential dynamics in the United States, for which census and sociological data is available, and show how trends in sociological surveys can be related to trends seen in racial segregation. In particular, we highlight that a social memory, akin to hysteresis in magnets, emerges in the segregation-integration transition even when individual agents have no memory. Beyond residential segregation, our work paves the way for systematic investigations of social-driven motility in real space from micro-organisms to humans, as well as fitness-mediated motion in more abstract genomic spaces.

The collective behavior of living organisms is the consequence of decisions taken by each organism in order to satisfy its needs, based on information collected on its environment. Despite this complexity, groups of organisms can display large, coherent patterns across space and time [1–31]. This regularity suggests that aspects of social behavior may be captured using the same kind of mathematical models used to describe inanimate physical systems such as fluids or solids, known as hydrodynamic theories [32–34]. By ignoring microscopic details in favor of describing behavior at large time- and length-scales, hydrodynamic theories capture universal features of emergent phenomena. This approach has been applied to biological systems ranging from microbial suspensions [35–43] and cellular tissues [44–55] to flocks of birds [3, 18, 56–58], pedestrian traffic [59–61], and runners in a marathon [62].

However, we lack a principled way of incorporating cognitive decision making into hydrodynamic models. Most work has focused on “social forces”, such as alignment, repulsion, or attraction, that mediate mechanical interactions between agents. Such forces can arise via effective steric interactions between individuals [63–65] or from various evolutionary pressures [17, 65–68], for instance to move efficiently in a flow or to avoid predation. These models do not account for decisions between options that are mechanically indistinguishable yet socially distinct – for instance, with whom to live [9, 69–78] or who to talk to [79, 80]. Similar issues also arise in cell fate decisions during development [81–83].

Here, we develop a data-driven pipeline to capture the physical manifestations of non-mechanical choices within a hydrodynamic theory. We take inspiration from microeconomics to codify individual preferences (micromotives)

into utility functions [84, 85], and then we incorporate them into a “sociohydrodynamic” theory that can account for collective behavior (macrobehavior).

We illustrate our approach on the case study of human residential dynamics in the United States, with a focus on segregation between non-Hispanic White and non-Hispanic Black residents [69, 86], for which data is readily available in the form of the US Census [87] and sociological research [88–91]. Our analysis suggests that global aspects of the dynamics of US population distributions can be described even with no precise knowledge of individual decisions, sidestepping the complex question of the origins and mechanisms behind segregation in the US [92–95].

Figure 1 summarizes our approach to construct a sociohydrodynamic theory relating micromotives to macrobehavior [70]. First, we identify candidate hydrodynamic variables and verify that they evolve slowly both in time and space (Fig. 1A). To be useful, the hydrodynamic variables must contain enough information to forecast their future values [96]. To test that, we use neural networks to learn a model-free rule for the evolution of population distributions (Fig. 1B). This also allows us to establish whether the dynamics are local (Fig. 1B). We then construct a microscopic theory that incorporates results from sociological surveys of individual preferences to estimate the social forces that lead to physical motion in the form of utility functions (Fig. 1C). Finally, we explicitly coarse-grain the microscopic dynamics to obtain our sociohydrodynamic equations, establishing links between individual utility functions and macroscopic patterns (Fig. 1D).

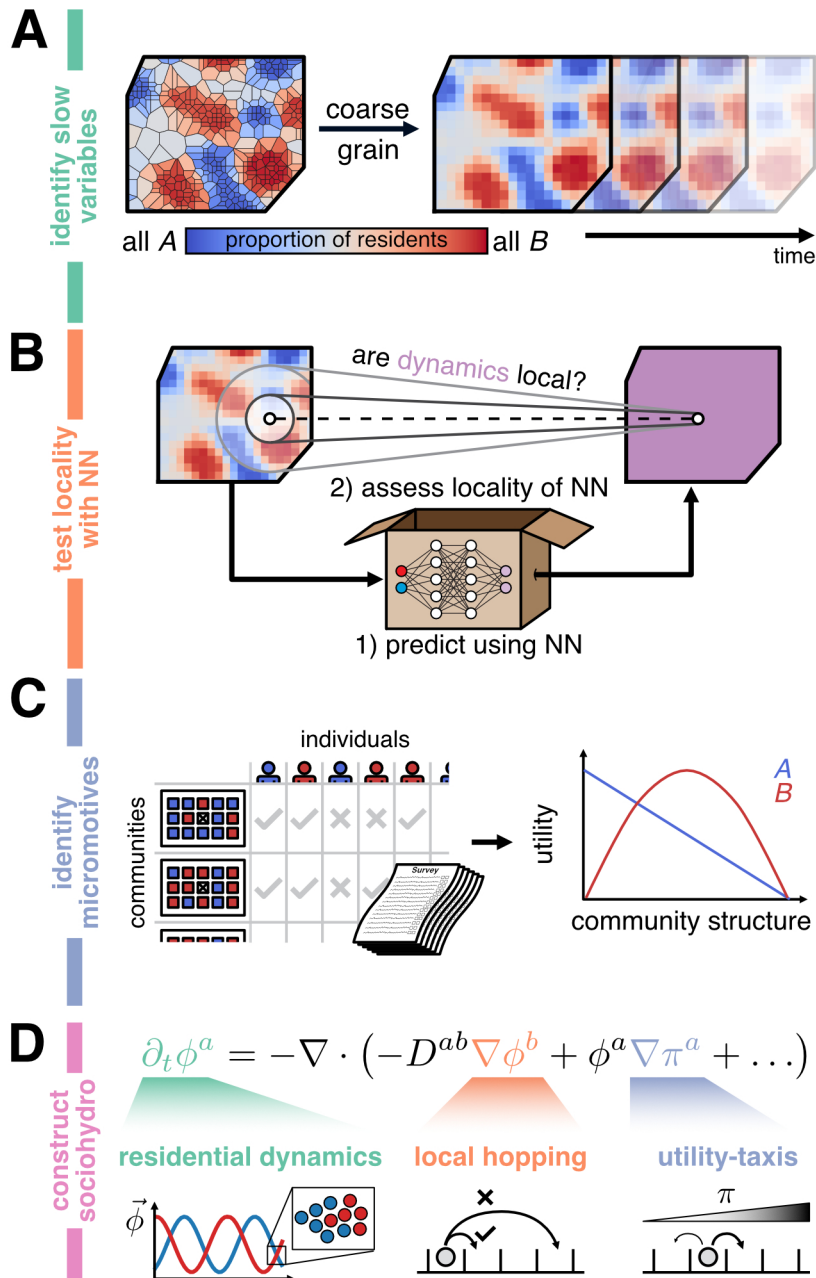


FIG. 1. **How to construct a sociohydrodynamic model from data.** (A) Illustration of a fictitious county split into census tracts. Colors represent the proportion of residents of each type in each census tract. The population distribution is coarse-grained onto a regular, square grid, and the dynamics of this coarse-grained field is then tracked in time. (B) Are the dynamics of population distributions determined locally? To answer this question, we first learn a dynamical rule for human residential dynamics directly from data using neural networks. Once the model is trained, we assess the locality of the learned dynamics. (C) (left) Sociological surveys ask individuals of different groups (red and blue) to give opinions on communities with different compositions of the groups. These choices are discretized into binary decisions, denoting a positive (\checkmark) or negative (\times) opinion of the proposed community. (right) We estimate a utility function as a function of the community structure based on the proportion of respondents of each type that give a positive assessment of that community. (D) Constructing our sociohydrodynamic model based on dynamics of $\vec{\phi}$ (green), with local dynamics (orange) and following spatial gradients of utility (purple).

I. THE SOCIOHYDRODYNAMIC PIPELINE

A. Identifying collective variables in social behavior

The first step towards building a hydrodynamic theory is to identify candidate collective variables. In our example of residential dynamics, a reasonable guess for collective variables are the populations of different groups, here White and Black individuals. In situations where the collective variables are not easy to guess, data-driven techniques can be used to aid the identification of suitable candidates [83, 96, 97]. In order to apply the usual tools of hydrodynamics, we must check that the collective variables are slowly varying both in space and time. In Fig. 2, we show data extracted from the US Census [87] – population numbers within a single county at the census tract level. We observe that the main features of the population distribution are unaffected by spatial coarse-graining, hinting at the existence of an intermediate length-scale over which the populations evolve (Fig. 2A). Quantitatively, White and Black populations distributions are correlated over distances four to seven times larger than the typical census tract ℓ in the region (Fig. 2B).

We also require hydrodynamic variables to vary slowly in time. Here, we assess the temporal change in populations via measurements of segregation. The absolute population numbers in different US counties show a variety of behaviors (SM). In order to focus on the effect of individual preferences on motility, we have ignored these changes, and focused on relative populations. Specifically, we use the divergence index, which measures how local racial composition differs from the global composition [98, 99] (see Methods for definition and SM for results using a different index). The spatial distribution of local segregation remains roughly constant over a span of 40 years, and its magnitude appears to diminish (Fig. 2C). The segregation index, defined as spatial sum of the local segregation (Methods), shows a slow decrease over 40 years, as measured previously [100–102] (Fig. 2D) [103]. By comparison, the typical time between individual moves is approximately 7 years [104].

Together, these two results verify that global aspects of human residential dynamics can indeed be described by collective variables that evolve slowly in both space and time. Formally, let us define the occupation fraction (or fill fraction) $\phi^a(\mathbf{r}, t) = n^a(\mathbf{r}, t)/\mathcal{N}(\mathbf{r})$ of group a at position \mathbf{r} at time t , in which $\mathcal{N}(\mathbf{r})$ is a carrying capacity (for instance, the number of existing homes in the area).

B. Assessing predictability and locality with neural networks

Next, we seek to assess the extent to which $\vec{\phi}$ are themselves predictive of future states of the system (Fig. 3A), and determine whether the dynamics are generated locally (Fig. 3B). Predictability refers to the idea that the collective variables contain sufficient information to predict

their own future state, a necessity for constructing any predictive theory. Locality, on the other hand, is a mathematical convenience more than a requirement. When it holds, it allows us to use a partial differential equation as a model, rather than an integro-differential equation. For human residential dynamics it is by no means guaranteed that changes in address would exhibit a bias towards nearby ones. In fact individual residential decisions manifestly need not exhibit any such constraints. Nonetheless, locality could still emerge at a sufficiently coarse-grained level and careful statistical analysis is needed to test this scenario. Similarly, in situations where motility occurs in abstract spaces rather than in physical space, like the evolution of genes, a test of locality would entail assessing the distance between sequences [105, 106], or a suitable alternative directly defined in terms of collective variables.

Testing the predictivity and locality of collective variables requires a reliable rule for dynamics, which we do not assume to have a priori. To address this issue, we train a convolutional neural network on US Census data to map the fields ϕ^a to the time derivatives of the fields $\partial_t \phi^a$ (Methods). We obtain a dynamical system

$$\partial_t \phi^a(\mathbf{r}, t) = f_{\otimes}^a[\vec{\phi}], \quad (1)$$

where f_{\otimes}^a represents a machine-learned dynamical rule for $\vec{\phi}$ (Fig. 3A). We then integrate Eq. (1) to obtain the population dynamics. Fig. 3B shows the results of the neural network prediction for four US counties, which correctly captures qualitative, large-scale features of the population distributions over a time-scale of 40 years. This indicates that current population fields are indeed sufficient to predict future populations.

To address the issue of locality, we consider the saliency (Methods)

$$\mathcal{K}^{ab}(|\mathbf{r} - \mathbf{r}'|) = \frac{\partial f_{\otimes}^a(\mathbf{r})}{\partial \phi^b(\mathbf{r}')}. \quad (2)$$

of the machine-learned dynamics, averaged over angles, which measures how much a model's predictions depend on its inputs [97, 107]. In essence, $\mathcal{K}^{ab}(r)$ measures how strongly the predicted evolution of ϕ^a at a certain point is influenced by the value of the field ϕ^b at a distance r from this point (Fig. 3C).

We emphasize that determining correlation lengths or similar quantities would not be sufficient to assess whether the dynamics is local. This can be understood from a simple example: an Ising model on a d -dimensional cubic lattice. Non-local interactions can induce long-range correlations, most strikingly in cases where local interactions cannot, such as when $d = 1$ [108]. However, non-locality is not necessary to induce long-range correlations. Indeed, the correlation length diverges at the critical point of the ferromagnet/paramagnet transition in $d \geq 2$ for the Ising model with nearest-neighbor (local) interactions. In summary, long-range correlation functions and local dynamical evolution are two disconnected properties.

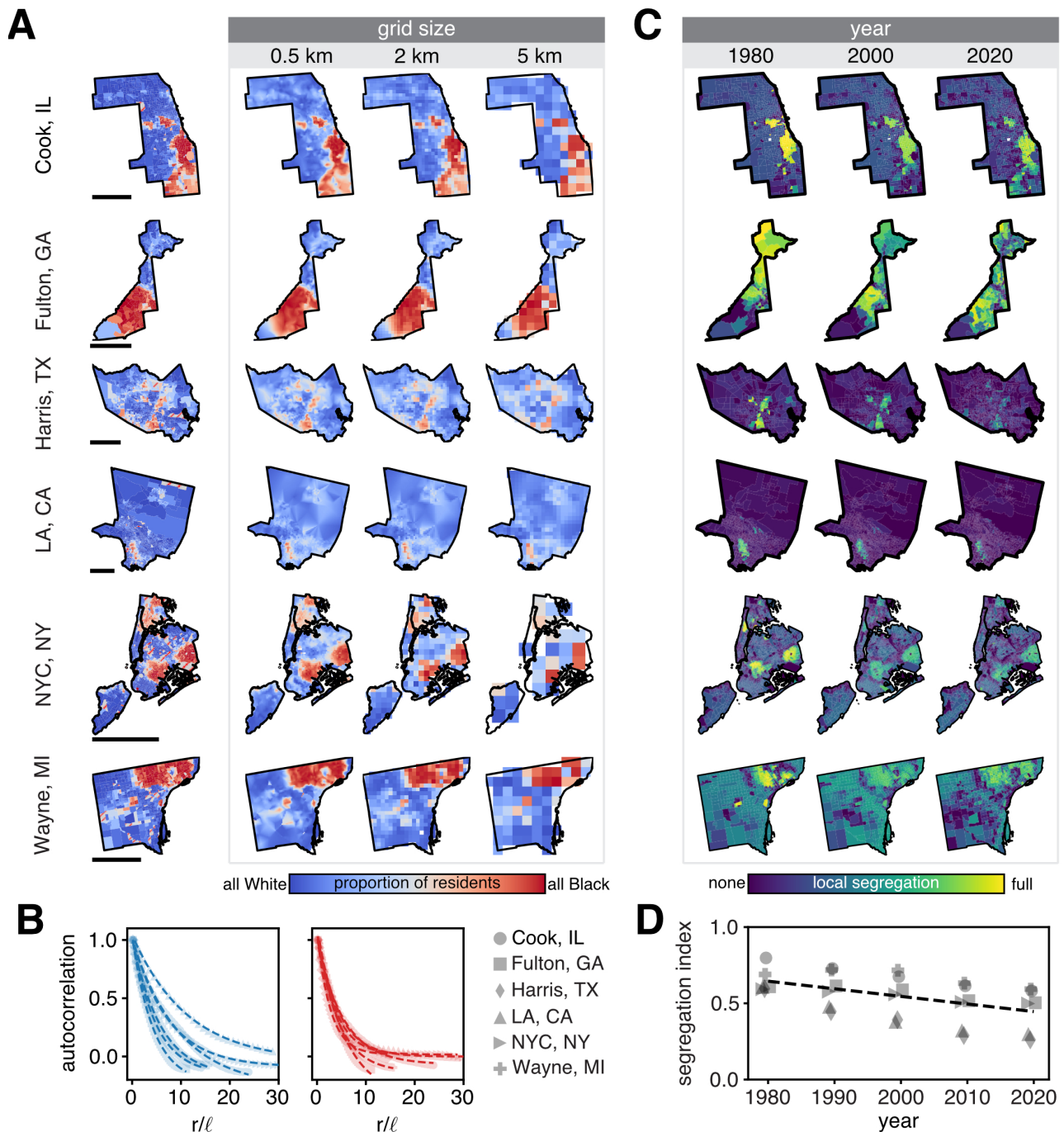


FIG. 2. Population distributions are slow variables across the US. (A) Results of interpolating populations in various regions around the US to grids of increasing size. From top to bottom, the regions are: Cook County IL, Fulton County GA, Harris County TX, Los Angeles County CA, New York City NY, and Wayne County MI. Colors represent the proportion of local populations that are non-Hispanic White (blue) and non-Hispanic Black (red). Scale bars are 25 km. (B) Autocorrelation functions for White (blue) and Black (red) populations in the six US regions in A (dots). Each set of data is fit to a decaying exponential (dashed line). The x-axis, measuring distance, is normalized by the median linear census tract size, ℓ of each region. Normalizing the correlation length by the ℓ accounts for differing densities, as each census tract is created to contain ~ 1000 residents. The typical correlation lengths for White and Black populations in the regions we analyzed are $\langle \xi_W \rangle = 7.3 \pm 2.5 \ell$ and $\langle \xi_B \rangle = 4.3 \pm 1.0 \ell$. (C) Local segregation for the six regions in A, shown from Census Data in 1980, 2000, and 2020. (D) Segregation index, measured as the weighted sum of the local segregation (Methods), for each region in C. Dashed line is a linear fit to all data.

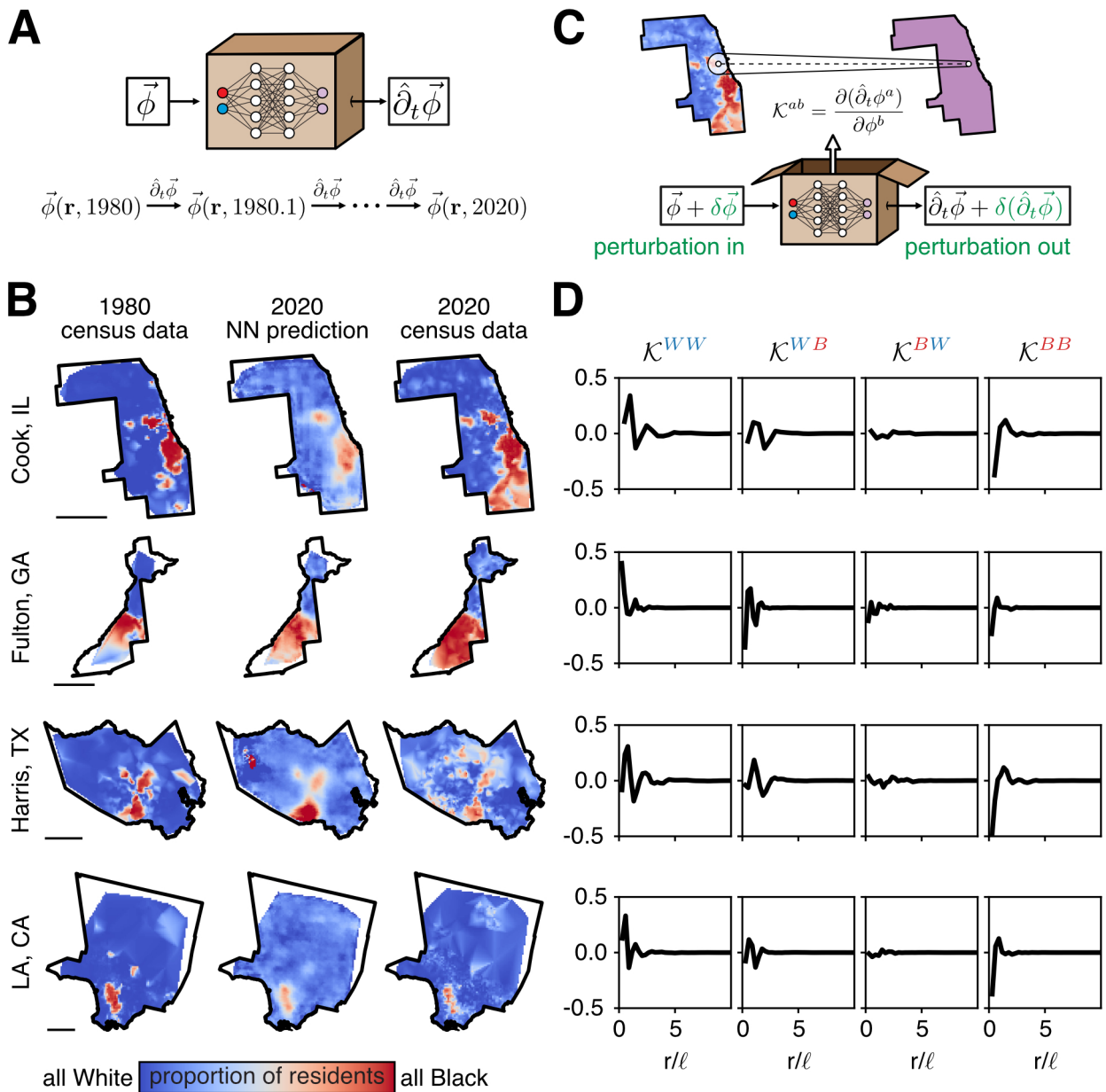


FIG. 3. **Human residential dynamics are local.** (A) Schematic illustration of dynamics of populations learned from Census data using neural networks. (B) Census data in 1980 (left) used as initial conditions for neural network predictions (middle), to be compared with 2020 Census data (right). Scale bars are 25 km. (C) Schematic illustration of saliency \mathcal{K}^{ab} as the linear response of the neural network. (D) Saliency measured radially for four regions, Cook County IL, Fulton County GA, Harris County TX, and Los Angeles County CA. Plots show mean (solid line) and standard deviation (shaded areas) from the four measurements.

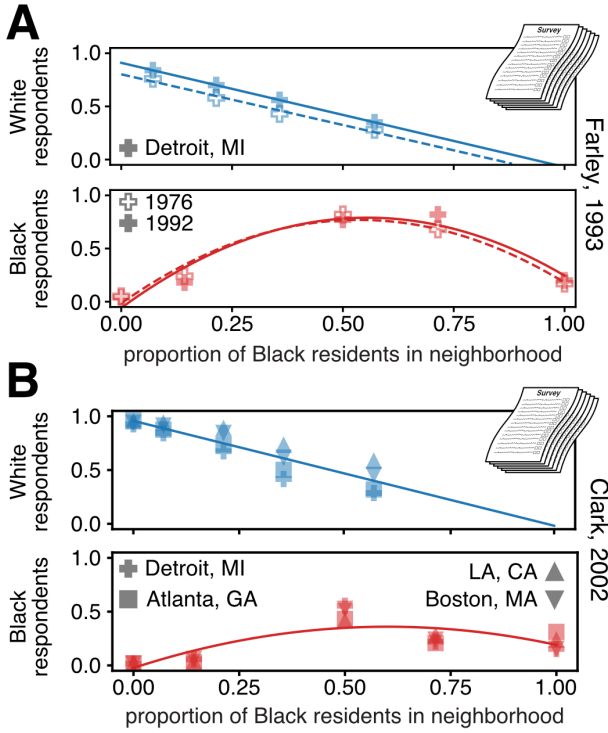


FIG. 4. **Persistent residential preferences from sociological surveys.** (A) Reproduction of survey results shown in Figs. 8 & 10 in Ref. [109]. Survey’s taken around Detroit, MI (+). Top plot shows proportion of White respondents “indicating they would be feel comfortable in the neighborhood” with the proportion of Black residents shown on the x-axis. Bottom shows proportion of Black residents ranking a neighborhood with the given proportion of Black residents as either their first or second choice among five options. Hollow circles show results from surveys taken in 1976, and filled circles show results from surveys taken in 1992. Dashed (1976) and solid (1992) lines are linear (top) and quadratic (bottom) fits to each set of data. (B) Reproduction of Figs. 4 & 7 in Ref. [110], which itself accumulates data from Ref. [111]. Surveys are taken in Detroit, MI (+), Atlanta, GA (■), Los Angeles, CA (▲), and Boston, MA (▼). Solid lines are linear (top) and quadratic (bottom) fits to each set of data.

Figure 3D shows the results for the saliency: \mathcal{K}^{ab} exhibits a similar structure for all regions, and is narrowly peaked at $r < 5\ell$. This indicates that f_{\otimes} only requires information within a very narrow region around each field in order to generate its dynamics. It is therefore plausible to attempt reproducing global features of US residential dynamics using a local field theory.

C. Extracting utility functions from social surveys.

In contrast with physical interactions, there is no consensus for models of human choices [112–118]. Economic approaches such as game theory describe decisions made by interacting rational agents. We adopt this framework here: agents attribute a quantity called utility to each

possible outcome of a decision, and tend to make decisions that maximize this utility [84, 119–121]. In the context of residential motility, the utility describes a person’s preferences in where to live. Here, we assume that the utility functions only depend on our hydrodynamic variables. This is the key feature of sociohydrodynamics: it establishes a feedback loop between the slowly evolving hydrodynamic variables and the utility functions capturing the decision-making that lead to motility in the first place.

The saliencies in Fig. 3C provide a first glimpse into the preferences of both groups, that appear to be similar across the US. In particular, \mathcal{K}^{WW} is mostly positive, while \mathcal{K}^{BB} is mostly negative. This suggests that utility functions could be directly inferred from data if no other way was available. In the case of humans, we can also ask individuals directly about their preferences, as it is routinely done in social surveys.

Figure 4A-B show typical results of such surveys reproduced from Refs. [109–111] which found that residential preferences remained consistent across a span of 16 years between 1976 and 1992 in the Detroit metropolitan area (panel A), and are also consistent in several major US metropolitan areas (panel B). The data points show the proportion of respondents that indicated a preference for a hypothetical neighborhood with the corresponding proportion of Black residents across time. White residents show a monotonic decrease in their preference of neighborhoods with increasing proportion of Black residents, with a statistically significant increase in the proportion of White respondents who indicate they would move into the neighborhoods regardless of the proportion of Black neighbors. On the other hand, Black residents show a marked preference for mixed neighborhoods, which remains consistent between the two surveys. Qualitatively similar results were obtained in other US-based surveys [75, 109, 110, 122, 123] (SM). Finally, we note that the survey data is qualitatively compatible with the saliencies measured from Census data in Fig. 3D. This leads us to infer that these survey results reflect an underlying utility function π^a for each group a , which are schematically represented by the continuous lines in Fig. 4A-B.

D. Constructing a hydrodynamic theory

We now incorporate all the elements extracted from data using the previous steps into a hydrodynamic model designed to capture universal features of residential dynamics found across US cities. Having identified the collective variables $\phi^a(\mathbf{r}, t)$ and verified that they are predictive of their own future, we write a general equation of motion for these variables

$$\partial_t \phi^a(\mathbf{r}, t) = -\nabla \cdot \mathbf{J}^a + S^a \quad (3a)$$

in which we have separated the dynamics into two parts: the divergence of a current \mathbf{J}^a redistributes the ϕ^a in

space without changing the total number of individuals in each group, while the source term S^a does change the total populations.

The locality of the dynamics (Fig. 3) motivates us to express $\mathbf{J}^a(\vec{\phi})$ as a function of $\vec{\phi}$ and their spatial derivatives

$$\mathbf{J}^a(\vec{\phi}) = \mathbf{v}^a \phi^a - D^{ab} \nabla \phi^b + \Gamma^{ab} \nabla^3 \phi^b. \quad (3b)$$

The first term in Eq. (3b) describes advection of ϕ^a at a velocity \mathbf{v}^a . Crucially, we assume that

$$\mathbf{v}^a = \nabla \pi^a(\vec{\phi}) \quad (3c)$$

is proportional to the gradient of the utility function, providing a link between motility and socioeconomic incentives. This reflects the propensity of individuals to move towards regions they prefer, up gradients in their utility. We call this behavior “utility-taxi”, in reference to chemotaxis [124] and infotaxis [125]. The second term in Eq. (3b) describes diffusion down gradients of the field ϕ^a , parameterized by the diffusion matrix D^{ab} . The third term acts like a surface tension, penalizing spatial gradients in ϕ^a [126, 127]. Note that both D^{ab} and Γ^{ab} may depend on $\vec{\phi}$. Given the slow spatial variation of the fields, we ignore higher order terms in the gradients. As should be the case for any flow of matter, we have only considered terms that make the current odd under spatial inversions, $\mathbf{J}^a(-\mathbf{r}) = -\mathbf{J}^a(\mathbf{r})$.

The source term in Eq. 3a describes how ϕ^a changes locally due to, for example, replication or death. For the remainder of this work, we will consider $S^a = 0$ in order to neglect absolute population changes (see SM). This allows us to focus on aspects of population dynamics that depend solely on individual preferences and choices, encompassed in the “economical” utility function π^a . Population changes are indeed observed in the US Census data (SM), but different trends are observed in different counties, motivating us to neglect these in a first approximation. In addition to human populations, these processes play a crucial role in contexts such as microbiology and ecology [10, 11, 41, 128–141]. Growth can be related to a local evolutionary “fitness function”, f^a , that describes to what extent the environment promotes the growth of a certain group [142–145]. Although the fitness and utility functions share similarities, they have no reason to be identical [41, 146, 147]. We discuss these aspects further in SM.

The coefficients D^{ab} and Γ^{ab} (that may be functions of the fields $\vec{\phi}$) could be learned using data-driven techniques that are agnostic to the underlying microscopic dynamics of social interactions. Here, we take a more principled approach: we construct and coarse-grain an agent-based model for residential dynamics, based on the Schelling model [9, 69–78], in which agents on a lattice randomly move to adjacent sites with a bias towards increasing their utility (SM). The coarse-graining (SM) leads to Eq. 54 with all coefficients expressed in terms of microscopic parameters, including the $\vec{\phi}$ -dependent D^{ab} and Γ^{ab} .

II. THE SOCIOHYDRODYNAMIC MODEL

A. A phase diagram for social behavior

Having obtained hydrodynamic equations for residential dynamics, Eq. (54), we can harness them to describe possible behaviors in the system. To do so, we consider a set of simplified utility functions π^a for two abstract groups $a = X, Y$ that are linear in the fields ϕ^a , represented in Fig. 5A,

$$\pi^a(\vec{\phi}) = \kappa^{ab} \phi^b(x, t). \quad (4)$$

These utility functions are designed to reflect a key feature of the empirical estimates shown in Fig. 1, namely that one increases as a function of ϕ^Y while the other decreases.

With this choice, the flux in Eq. 3b becomes

$$J^a(\vec{\phi}) = (-D^{ab} + \kappa^{ab}) \nabla \phi^b + \Gamma^{ab} \nabla^3 \phi^b.$$

This results in diffusion of ϕ^a either up or down gradients of ϕ^b , depending on the symmetries of the matrix κ^{ab} (Fig. 5C, top). Based on known results on the Schelling model [9, 69–74], we expect to observe segregation (where the two groups concentrate at different places) and integration (where the two groups occupy mainly the same place), depending on the utility functions.

For every utility function, we solve Eq. (54) numerically, and then report the resulting dynamical phase of the system in Fig. 5B, where each color represents a qualitatively different state (see SM for criteria used in the categorization). We indeed observe the expected static states of segregation and integration (purple and green regions). In addition, we observe an additional time-dependent steady-state in which both groups continuously migrate (orange region). Similar states have recently been reported in Ref. [78]. Finally, there are coexistence regions (light green) where multiple phases are observed depending on the initial state of the system.

The basic mechanism leading to the migratory states in Fig. 5 is as follows. Figure 5A shows that the utility of X increases when the fraction of Y *decreases*, whereas the utility of Y increases when the fraction of X *increases*. In other words, Y tends to move towards X while X tends to move away from Y , which leads to a continued motion.

Mathematically, the utilities π^X and π^Y are incompatible, in the sense that $\partial \pi^Y / \partial \phi^X \neq \partial \pi^X / \partial \phi^Y$. As a consequence, the interaction between X and Y is non-reciprocal [148–159]. Migratory states can only arise when the compatibility condition is violated. When it is satisfied, it is possible to cast the dynamics as a gradient descent in a high-dimensional space (SM and Refs. [9, 148, 156, 160]), thereby excluding time-dependent steady states like travelling waves.

We also find that migration depends on the initial state of the population distributions. In Fig. 5C, we observe that each of the two populations is spatially concentrated in a bump. In the SM, we show that no migration occurs when the overlap between the populations is below

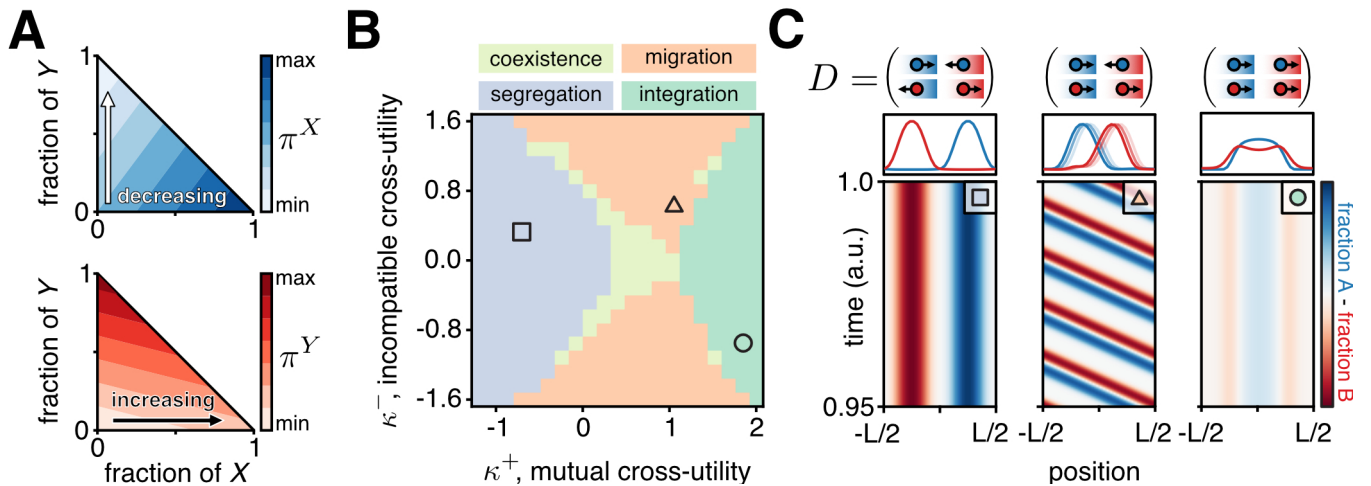


FIG. 5. **Sociohydrodynamic model.** (A) Linear utility functions for the two groups in our hydrodynamics model, $\pi^X(\phi^X, \phi^Y) = \kappa^{XX}\phi^X + \kappa^{XY}\phi^Y$ and $\pi^Y(\phi^X, \phi^Y) = \kappa^{YX}\phi^X + \kappa^{YY}\phi^Y$, shown in the left and right subpanels, respectively. Plots show mutual cross-utility coefficient $\kappa^+ = \kappa^{XY} + \kappa^{YX} = -0.5$, incompatible cross-utility coefficient $\kappa^- = \kappa^{YX} - \kappa^{XY} = 1$, and self-utility $\kappa^{XX} = \kappa^{YY} = 1$. (B) Phase diagram showing different possible steady state dynamics depending on mutual and incompatible cross-utility coefficients, κ^\pm . We see 4 phases: segregation (purple), migration (orange), integration (green), and coexistence of two phases (yellow). (C) Kymographs for steady state dynamics in the segregated phase, $(\kappa^+, \kappa^-) = (-0.07, 0.02)$ (left), migrating phase, $(\kappa^+, \kappa^-) = (0.02, 0.04)$ (middle), and integrated phase, $(\kappa^+, \kappa^-) = (0.09, -0.06)$ (right). Plots on the top show the state of the system at the final time. Schematics of the resulting diffusion matrix shown on top of each phase. We set $T = 0.1$ and the average fill fraction of both types to be $\langle \phi^X \rangle = \langle \phi^Y \rangle = 0.25$.

a threshold value. As the two bumps overlap (like in Fig. 5C), the populations interact and generate motion.

B. Emergent history-dependence of desegregation

With a precise mapping of microscopic preferences to macroscopic behavior, one can probe the effects of changing preferences. In a microbiological context, these changes could result from evolution, as is the case, for instance, in a bacterial strain adapting to metabolize a new carbon source. In a sociological context, they could result from the transformation of cultural attitudes.

Thus, we now ask: can a change in preferences lead to decreased segregation? Survey results across sixteen years show an evolution in utility functions [109]: White respondents have become more comfortable in neighborhoods with a given proportion of Black residents (Fig. 4). In addition, analysis of the Census data in Figs. 2C-D indicates a slow decrease in the measured segregation across the US. To connect these two observations, we use utility functions inspired from Fig. 4 in our sociohydrodynamic theory to directly test how changing preferences affects segregation.

We take π^X to be a linearly decreasing function of the local proportion of Y , reflecting the sociological findings of White respondents. Similarly, we take π^Y to be a quadratic function of the local proportion of Y , reflecting the sociological findings of Black respondents. We then solve the sociohydrodynamic equation (54) for linear utilities π^X with different slopes. In Fig. 6B, we plot the

segregation index measured in the resulting steady-state as a function of the slope (grey dots). We indeed find that steeper slopes for White preferences lead to larger levels of segregation, reproducing the trend observed in the measured segregation in US cities (purple lines in the figures are obtained by the linear fit in Fig. 2D).

The presence of coexistence regions in Fig. 5C suggests that a set of preferences can support multiple states of segregation. Which state is selected depends on the history of the system, even when individuals have no memory and are not artificially hampered from moving in certain neighborhoods. To demonstrate this with our measured utility functions, we consider slowly changing preferences of both groups over time. This externally imposed change can be interpreted, for example, as the result of campaigns designed to mitigate segregation, run by governments or non-governmental organizations (NGOs).

Specifically, we implement a cycle in the slope of π^X , starting and ending with the same value. The segregation indices measured in the resulting simulations are shown in Fig. 6C. Strikingly, some preferences (x-axis of the plot) correspond to two different segregation indices, depending on whether this preference is reached from a segregated or a mixed state. This phenomenon is known as hysteresis: the state of the system depends on its past [161]. This is a form of socioeconomic memory that emerges at the community level, despite the fact that the individuals themselves have no memory within our model. This means that two communities, with an identical set of preferences, can be segregated or integrated depending on their histories. From the perspective of public policy,

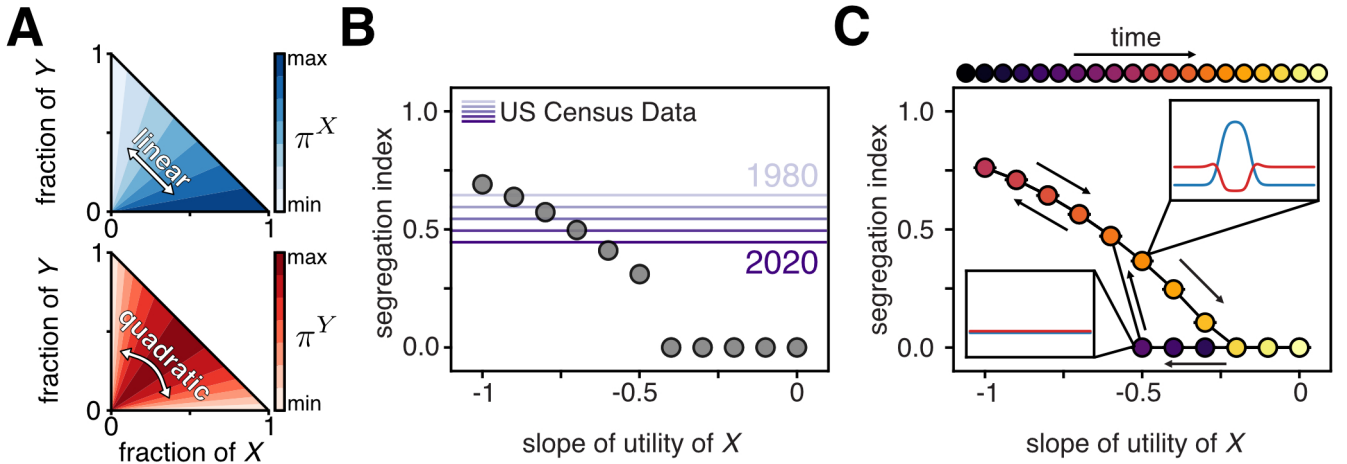


FIG. 6. **Trends and history dependence of segregation.** (A) Inspired by the trends in residential preferences illustrated in Fig. 4, we consider two utility functions as a function of proportion of residents. Utility of type X is monotonic, decreasing as the proportion of type Y increases (blue). The utility of type Y is non-monotonic, exhibiting a preference for mixed communities. We capture the changing trends in π^X by adjusting its slope, changing the strength of the preference for neighborhoods of a specific composition. (See Eq. (10) for expressions, in which the slope is called c .) (B) Dots show measured segregation indices for 10 independent simulations run for the given slope of π^X . Purple lines show the measured segregation indices from the US Census data in each decade, as given by the linear regression in (B). Every simulation here is run starting from an initially homogeneous set of population distributions. (C) Segregation index for $n = 10$ simulations where π^X is changed slowly. Starting with a constant π^X , we run simulations until a steady state is reached. Then, we change the slope of π^X by a small amount (here, by 0.1), and continue the simulations until a new steady state is reached. We repeat this process for a full cycle of the slope, beginning and ending with the slope of zero for π^X .

our results suggest that segregation could be reduced in a city or country without changing the personal preferences of its inhabitants.

III. DISCUSSION AND OUTLOOK

To sum up, we have introduced a data-driven pipeline to construct hydrodynamic descriptions of social motility. We have illustrated this framework on the example of racial segregation in human residential dynamics. Our work neglects well-documented economic and institutional barriers to residential choices [86, 93, 109, 111, 162–167]. By doing so, we show that segregation can persist even in the absence of both institutional barriers and segregative preferences, due to an emergent memory in the population of memoryless agents.

More broadly, our work illustrates how a hydrodynamic theory of collective social motility can provide a precise mathematical mapping from micromotives to macrobehavior [70]. Social motility is not unique to humans, with microbiology offering perhaps the most quantitatively studied examples [168–173]. Indeed, microorganisms adjust their collective motility by sensing each other or the external environment in a process known as quorum sensing [174, 175]. The utility-taxis performed by the socioeconomic agents in Eq. 3c generalizes the chemotaxis by motile microorganisms [146, 147, 176, 177]. Our *in silico* experiment of slowly varying utility functions could

be adapted in this context to investigate the effects of directed evolution [178–180] on a population. This connection also introduces another intriguing possibility, which is to study the spontaneous evolution/adaptation of social preferences, analogously to microorganismic adaptation in time-varying environments [181–183].

Finally, one could also apply our approach to characterize motion through abstract (rather than physical) spaces. For instance, the coevolution of viruses and immune responses is often modeled to occur in an antigenic space parameterized by the cross-reactivity in pathogen-host interactions [106, 184]. Such interactions are manifestly non-reciprocal, with immune systems attempting to occupy the same space as viruses, while viruses attempt to escape. In such a case, the migratory phase in Fig. 5 would become relevant as a manifestation of viral evolution and escape.

Acknowledgements. DS, MF, and YA acknowledge support from a MRSEC-funded Kadanoff–Rice fellowship and the University of Chicago Materials Research Science and Engineering Center, which is funded by the National Science Foundation under award no. DMR-2011854. YA acknowledges support from the Zuckerman STEM Leadership Program. JC acknowledges support from the National Science Foundation under grant DMR-2118415. DM acknowledges support from the Enrico Fermi Institute and the Kadanoff Center at UChicago. JC and MF acknowledge support from the National Science Foundation under grant DMR-2118415. MF and

VV acknowledge partial support from the UChicago Materials Research Science and Engineering Center (NSF DMR-2011864). MF acknowledges support from the Simons Foundation. VV acknowledges support from the Army Research Office under grant W911NF-22-2-0109 and W911NF-23-1-0212 and the Theory in Biology program of the Chan Zuckerberg Initiative. This research was supported from the National Science Foundation through the Center for Living Systems (grant no. 2317138). This work was completed in part with resources provided by the University of Chicago's Research Computing Center.

IV. METHODS

A. US Census Data.

The US population data are decennial census data at the census tract level for decades 1980-2010, collected using the IPUMS database [87]. GIS file information, as well as details on interpolation procedure, are provided in the SM.

B. Segregation Indices

In order to quantify both the measured distribution of human populations as well as our simulations, we utilize the so-called entropy index, which measures Kullback-Leibler divergence between the demographic distribution in each census tract and the demographic distribution of the entire region. Details are given in the SM.

C. Sociohydrodynamic diffusion matrix.

We provide the full derivation of our sociohydrodynamic theory in the SI, including the effects of altruism. Here, we simply report the diffusion matrix in Eq. 54. Assuming that the utility does not have an explicit spatial dependence, i.e. $\pi^a = \pi^a(\vec{\phi})$, we have

$$J^a(x, t) = - \sum_b D^{ab} \partial_x \phi^b + \phi^a \partial_x \pi^a + \Gamma^{ab} \partial_x^3 \phi^b \quad (5)$$

$$= - \sum_b \mathbb{D}^{ab} \partial_x \phi^b + \Gamma^{ab} \partial_x^3 \phi^b \quad (6)$$

where \mathbb{D}^{ab} are elements of the matrix

$$\mathbb{D}(\vec{\phi}) = T \begin{pmatrix} 1 - \phi^Y & \phi^X \\ \phi^Y & 1 - \phi^X \end{pmatrix} - (1 - \phi^X - \phi^Y) \begin{pmatrix} \phi^X \frac{\partial \pi^X}{\partial \phi^X} & \phi^X \frac{\partial \pi^X}{\partial \phi^Y} \\ \phi^Y \frac{\partial \pi^Y}{\partial \phi^X} & \phi^Y \frac{\partial \pi^Y}{\partial \phi^Y} \end{pmatrix}. \quad (7)$$

The first term arises due to volume exclusion effects with finite carrying capacity of the lattice sites in the agent-based model. The second term arises from the utility functions. Similarly, we find

$$\Gamma^{ab} = \delta^{ab} \phi^b (1 - \phi^X - \phi^Y), \quad (8)$$

where δ^{ab} is the Kronecker delta.

D. Simulation methods.

We simulate Eq. 54 in 1 spatial dimension using a finite difference method, with a 4th order discretization in space and 1st order discretization in time. Unless otherwise stated, we set $T = 0.1$ and $\Gamma = 1$, and use a time step of $\Delta t = 0.1$ and $\Delta x = 0.625$.

E. Linear utility functions.

The linear utility functions used in Fig. 5 are given by

$$\pi^a(\vec{\phi}) = \sum_b \kappa^{ab} \phi^b \quad (9a)$$

$$\kappa = \begin{pmatrix} \kappa^{XX} & \kappa^{XY} \\ \kappa^{YX} & \kappa^{YY} \end{pmatrix} \quad (9b)$$

The matrix elements κ^{ab} quantify how the utility of a is affected by the presence of b . We call κ^{XX} and κ^{YY} the self-utility coefficients, and κ^{XY} and κ^{YX} the cross-utility coefficients. We find it convenient to define $\kappa^\pm = \kappa^{YX} \pm \kappa^{XY}$. We dub κ^+ the ‘‘mutual’’ cross-utility coefficient as it measures the degree of mutual (dis)like between the X and Y . Likewise, we call κ^- the ‘‘incompatible’’ cross-utility coefficient as it measures the incompatibility of the two utilities with each other (see Fig. 5).

F. Empirical utility functions.

In Figure 6A of the main text, we construct utility functions that are inspired by the survey results. In the SI, we show examples from two other surveys that, in addition to the results shown in Fig. 4, support the qualitative features of our empirical utility functions – namely that the utility of type X is a monotonically decreasing utility with the proportion of type Y , while the utility of type Y is peaked for mixed neighborhoods

In all cases, surveys asked respondents to rank neighborhoods in terms of the proportion of Black residents. As a result, we assume our empirical utilities to be functions of the proportion of type Y . Let $\varphi^a(x, t) = \phi^a / (\phi^X + \phi^Y)$ be the fractional proportion of type a at location x and time t . We define

$$\begin{aligned} \pi^X(\phi^X, \phi^Y) &= \pi^X(\varphi^Y) = 1 - c \varphi^Y \\ \pi^Y(\phi^X, \phi^Y) &= \pi^Y(\varphi^Y) = 4\varphi^Y(1 - \varphi^Y). \end{aligned} \quad (10)$$

In the above, c is a parameter controlling the slope of the preference of type X individuals. These are the functions plotted in Fig. 6 of the main text.

Preference protocol. To perform the slow changes in preferences presented in Fig. 6C, we run $N = 10$ simulations of Eq. 54 with $c = 0$ until a steady state is reached at $t = t_{ss}$. We then take each $(\phi^A(x, t_{ss}), \phi^B(x, t_{ss}))$ as the initial condition for a new simulation with $c = 0.1$, and run it for an additional time t_{ss} . We repeat this process for $c = \{0, 0.1, \dots, 0.9, 1.0, 0.9, \dots, 0.1, 0\}$. In these simulations, we set $T = 0.1$, $\Gamma = 1$, $L = 60$, and $t_{ss} = 2.5 \times 10^5$.

G. Assessing locality via neural networks

We used a convolutional neural network to predict the dynamics $(\partial_t \phi^W, \partial_t \phi^B)$ from an initial condition

(ϕ^W, ϕ^B) . Briefly, it contains two convolutional modules which compute latent features at the scale of the input data and using a downsampled representation in order to aggregate spatial information over short or long distances. A FEM solver integrates the predicted derivatives on the county mesh, and the network learns to minimize the difference between its predictions and census data, following the physical bottleneck approach outlined in [97]. The full network details are given in the SI.

We used the trained network to predict population dynamics over the 40-year window spanned by decennial Census data. We do this using a finite element method implemented in Fenics, where the neural network provides the time derivative at each time step. To assess locality in the predicted dynamics, we computed the output saliencies for the trained network. Saliency is a measure of how much a model’s predictions depend on its inputs and is here defined as [107]

$$K^{ab}(\mathbf{r}_i, \mathbf{r}_j) = \frac{\partial(\partial_t \hat{\phi}^a(\mathbf{r}_i))}{\partial \phi^b(\mathbf{r}_j)} \quad (11)$$

Here a, b are population indices while i, j refer to spatial coordinates within each county. We compute $K^{ab}(\mathbf{r}_i, \mathbf{r}_j)$ from each input-output pair in each county dataset, for 100 randomly sampled output points \mathbf{r}_i and all input points \mathbf{r}_j . We azimuthally average this into a set of curves $K^{ab}(|\mathbf{r}_a - \mathbf{r}_b|)$ which are plotted in Figure 1.

-
- [1] H. Blumer, Social problems as collective behavior, *Social Problems* **18**, 298 (1971).
- [2] D. Helbing and P. Molnár, Social force model for pedestrian dynamics, *Physical Review E* **51**, 4282 (1995).
- [3] R. L. Hughes, The flow of human crowds, *Annual Review of Fluid Mechanics* **35**, 169 (2003).
- [4] A. Treuille, S. Cooper, and Z. Popović, Continuum crowds, *ACM Transactions on Graphics* **25**, 1160 (2006).
- [5] D. Sumpter, The principles of collective animal behaviour, *Philosophical Transactions of the Royal Society B: Biological Sciences* **361**, 5 (2005).
- [6] L. Bettencourt and G. West, A unified theory of urban living, *Nature* **467**, 912 (2010).
- [7] L. M. A. Bettencourt, The origins of scaling in cities, *Science* **340**, 1438 (2013).
- [8] M. Schlöpfer, L. Dong, K. O’Keeffe, P. Santi, M. Szell, H. Salat, S. Anklesaria, M. Vazifeh, C. Ratti, and G. B. West, The universal visitation law of human mobility, *Nature* **593**, 522 (2021).
- [9] S. Grauwin, E. Bertin, R. Lemoy, and P. Jensen, Competition between collective and individual dynamics, *Proceedings of the National Academy of Sciences* **106**, 20622 (2009).
- [10] O. Hallatschek, P. Hersen, S. Ramanathan, and D. R. Nelson, Genetic drift at expanding frontiers promotes gene segregation, *Proceedings of the National Academy of Sciences* **104**, 19926 (2007).
- [11] T. Reichenbach, M. Mobilia, and E. Frey, Mobility promotes and jeopardizes biodiversity in rock–paper–scissors games, *Nature* **448**, 1046 (2007).
- [12] E. Frey, Evolutionary game theory: Theoretical concepts and applications to microbial communities, *Physica A: Statistical Mechanics and its Applications* **389**, 4265 (2010).
- [13] G. J. Stephens, M. B. de Mesquita, W. S. Ryu, and W. Bialek, Emergence of long timescales and stereotyped behaviors in *Caenorhabditis elegans*, *Proceedings of the National Academy of Sciences* **108**, 7286 (2011).
- [14] I. D. Couzin and J. Krause, Self-organization and collective behavior in vertebrates, in *Advances in the Study of Behavior* (Elsevier, 2003) pp. 1–75.
- [15] I. D. Couzin, J. Krause, N. R. Franks, and S. A. Levin, Effective leadership and decision-making in animal groups on the move, *Nature* **433**, 513 (2005).
- [16] C. W. Reynolds, Flocks, herds and schools: A distributed behavioral model, in *Proceedings of the 14th annual conference on Computer graphics and interactive techniques* (ACM, 1987).
- [17] M. Ballerini, N. Cabibbo, R. Candelier, A. Cavagna, E. Cisbani, I. Giardina, V. Lecomte, A. Orlandi, G. Parisi, A. Procaccini, M. Viale, and V. Zdravkovic, Interaction ruling animal collective behavior depends on topological rather than metric distance: Evidence from a field study, *Proceedings of the National Academy of Sciences* **105**, 1232 (2008).
- [18] T. Vicsek and A. Zafeiris, Collective motion, *Physics Reports* **517**, 71 (2012).
- [19] M. C. Marchetti, J.-F. Joanny, S. Ramaswamy, T. B. Liverpool, J. Prost, M. Rao, and R. A. Simha, Hydrodynamics of soft active matter, *Reviews of Modern Physics* **85**, 1143 (2013).
- [20] J. Adler, Chemotaxis in bacteria, *Science* **153**, 708 (1966).
- [21] E. F. Keller and L. A. Segel, Traveling bands of chemotactic bacteria: A theoretical analysis, *Journal of Theoretical Biology* **30**, 235 (1971).
- [22] F. Ginelli, F. Peruani, M.-H. Pillot, H. Chaté, G. Theraulaz, and R. Bon, Intermittent collective dynamics emerge from conflicting imperatives in sheep herds, *Proceedings of the National Academy of Sciences* **112**, 12729 (2015).
- [23] O. Peleg, J. M. Peters, M. K. Salcedo, and L. Mahadevan, Collective mechanical adaptation of honeybee swarms, *Nature Physics* **14**, 1193 (2018).
- [24] S. A. Ocko, A. Heyde, and L. Mahadevan, Morphogenesis of termite mounds, *Proceedings of the National Academy of Sciences* **116**, 3379 (2019).
- [25] J. B. Bak-Coleman, M. Alfano, W. Barfuss, C. T. Bergstrom, M. A. Centeno, I. D. Couzin, J. F. Donges, M. Galesic, A. S. Gersick, J. Jacquet, A. B. Kao, R. E. Moran, P. Romanczuk, D. I. Rubenstein, K. J. Tombak, J. J. V. Bavel, and E. U. Weber, Stewardship of global collective behavior, *Proceedings of the National Academy of Sciences* **118**, 10.1073/pnas.2025764118 (2021).
- [26] D. H. Kelley and N. T. Ouellette, Emergent dynamics of laboratory insect swarms, *Scientific Reports* **3**, 10.1038/srep01073 (2013).
- [27] R. Ni, J. G. Puckett, E. R. Dufresne, and N. T. Ouellette, Intrinsic fluctuations and driven response of insect swarms, *Physical Review Letters* **115**, 118104 (2015).
- [28] R. Ni and N. T. Ouellette, On the tensile strength of insect swarms, *Physical Biology* **13**, 045002 (2016).
- [29] N. T. Ouellette, A physics perspective on collective animal behavior, *Physical Biology* **19**, 021004 (2022).
- [30] A. Corbetta and F. Toschi, Physics of human crowds, *Annual Review of Condensed Matter Physics* **14**, 311 (2023).
- [31] W. Van Saarloos, V. Vitelli, and Z. Zeravcic, *Soft Matter: Concepts, Phenomena and Applications*. (Princeton University Press, 2023).
- [32] L. P. Kadanoff and P. C. Martin, Hydrodynamic equations and correlation functions, *Annals of Physics* **24**, 419 (1963).
- [33] L. D. Landau and E. M. Lifshitz, *Fluid Mechanics : Landau and Lifshitz* (Elsevier Science & Technology Books, 1987) p. 539.
- [34] P. W. Anderson, More is different, *Science* **177**, 393 (1972).
- [35] A. Sokolov, I. S. Aranson, J. O. Kessler, and R. E. Goldstein, Concentration Dependence of the Collective Dynamics of Swimming Bacteria, *Physical Review Letters* **98**, 158102 (2007).
- [36] I. S. Aranson, A. Sokolov, J. O. Kessler, and R. E. Goldstein, Model for dynamical coherence in thin films of self-propelled microorganisms, *Physical Review E* **75**, 040901 (2007).
- [37] A. Celani and M. Vergassola, Bacterial strategies for chemotaxis response, *Proceedings of the National Academy of Sciences* **107**, 1391 (2010).
- [38] C. Liu, X. Fu, L. Liu, X. Ren, C. K. Chau, S. Li, L. Xiang, H. Zeng, G. Chen, L.-H. Tang, P. Lenz, X. Cui, W. Huang, T. Hwa, and J.-D. Huang, Sequential estab-

- ishment of stripe patterns in an expanding cell population, *Science* **334**, 238 (2011).
- [39] H. H. Wensink, J. Dunkel, S. Heidenreich, K. Drescher, R. E. Goldstein, H. Löwen, and J. M. Yeomans, Mesoscale turbulence in living fluids, *Proceedings of the National Academy of Sciences* **109**, 14308 (2012).
- [40] H. Wioland, F. G. Woodhouse, J. Dunkel, J. O. Kessler, and R. E. Goldstein, Confinement stabilizes a bacterial suspension into a spiral vortex, *Physical Review Letters* **110**, 268102 (2013).
- [41] J. Cremer, T. Honda, Y. Tang, J. Wong-Ng, M. Vergasola, and T. Hwa, Chemotaxis as a navigation strategy to boost range expansion, *Nature* **575**, 658 (2019).
- [42] K. Copenhagen, R. Alert, N. S. Wingreen, and J. W. Shaevitz, Topological defects promote layer formation in *myxococcus xanthus* colonies, *Nature Physics* **17**, 211 (2020).
- [43] A. I. Curatolo, N. Zhou, Y. Zhao, C. Liu, A. Daerr, J. Tailleur, and J. Huang, Cooperative pattern formation in multi-component bacterial systems through reciprocal motility regulation, *Nature Physics* **16**, 1152 (2020).
- [44] A. F. Mertz, S. Banerjee, Y. Che, G. K. German, Y. Xu, C. Hyland, M. C. Marchetti, V. Horsley, and E. R. Dufresne, Scaling of traction forces with the size of cohesive cell colonies, *Physical Review Letters* **108**, 198101 (2012).
- [45] T. B. Saw, A. Doostmohammadi, V. Nier, L. Kocgozlu, S. Thampi, Y. Toyama, P. Marcq, C. T. Lim, J. M. Yeomans, and B. Ladoux, Topological defects in epithelia govern cell death and extrusion, *Nature* **544**, 212 (2017).
- [46] T. Ruiz-Herrero, K. Alessandri, B. V. Gurchenkov, P. Nassoy, and L. Mahadevan, Organ size control via hydraulically gated oscillations, *Development* **144**, 4422 (2017).
- [47] C. Pérez-González, R. Alert, C. Blanch-Mercader, M. Gómez-González, T. Kolodziej, E. Bazellieres, J. Casademunt, and X. Trepat, Active wetting of epithelial tissues, *Nature Physics* **15**, 79 (2018).
- [48] G. Duclos, C. Blanch-Mercader, V. Yashunsky, G. Salbreux, J.-F. Joanny, J. Prost, and P. Silberzan, Spontaneous shear flow in confined cellular nematics, *Nature Physics* **14**, 728 (2018).
- [49] S. J. Streichan, M. F. Lefebvre, N. Noll, E. F. Wieschaus, and B. I. Shraiman, Global morphogenetic flow is accurately predicted by the spatial distribution of myosin motors, *eLife* **7**, 10.7554/elife.27454 (2018).
- [50] R. Alert, C. Blanch-Mercader, and J. Casademunt, Active fingering instability in tissue spreading, *Physical Review Letters* **122**, 088104 (2019).
- [51] S. Banerjee and M. C. Marchetti, Continuum models of collective cell migration, in *Cell Migrations: Causes and Functions* (Springer International Publishing, 2019) pp. 45–66.
- [52] D. Boockock, N. Hino, N. Ruzickova, T. Hirashima, and E. Hannezo, Theory of mechanochemical patterning and optimal migration in cell monolayers, *Nature Physics* **17**, 267 (2020).
- [53] M. S. Yousafzai, V. Yadav, S. Amiri, M. F. Staddon, Y. Errami, G. Jaspard, S. Banerjee, and M. Murrell, Cell-matrix elastocapillary interactions drive pressure-based wetting of cell aggregates, *Physical Review X* **12**, 031027 (2022).
- [54] J.-M. Armengol-Collado, L. N. Carenza, J. Eckert, D. Krommydas, and L. Giomi, Epithelia are multiscale active liquid crystals, *Nature Physics* **19**, 1773 (2023).
- [55] M. Serra, G. Serrano Nájera, M. Chuai, A. M. Plum, S. Santhosh, V. Spandan, C. J. Weijer, and L. Mahadevan, A mechanochemical model recapitulates distinct vertebrate gastrulation modes, *Science Advances* **9**, 10.1126/sciadv.adh8152 (2023).
- [56] T. Vicsek, A. Czirók, E. Ben-Jacob, I. Cohen, and O. Shochet, Novel type of phase transition in a system of self-driven particles, *Physical Review Letters* **75**, 1226 (1995).
- [57] J. Toner and Y. Tu, Flocks, herds, and schools: A quantitative theory of flocking, *Physical Review E* **58**, 4828 (1998).
- [58] A. Cavagna and I. Giardina, Bird flocks as condensed matter, *Annual Review of Condensed Matter Physics* **5**, 183 (2014).
- [59] D. Helbing, Traffic and related self-driven many-particle systems, *Reviews of Modern Physics* **73**, 1067–1141 (2001).
- [60] A. Corbetta, J. A. Meeusen, C.-m. Lee, R. Benzi, and F. Toschi, Physics-based modeling and data representation of pairwise interactions among pedestrians, *Physical Review E* **98**, 062310 (2018).
- [61] J. L. Silverberg, M. Bierbaum, J. P. Sethna, and I. Cohen, Collective motion of humans in mosh and circle pits at heavy metal concerts, *Physical Review Letters* **110**, 228701 (2013).
- [62] N. Bain and D. Bartolo, Dynamic response and hydrodynamics of polarized crowds, *Science* **363**, 46 (2019).
- [63] D. Helbing, I. Farkas, and T. Vicsek, Simulating dynamical features of escape panic, *Nature* **407**, 487 (2000).
- [64] D. Geyer, D. Martin, J. Tailleur, and D. Bartolo, Freezing a flock: Motility-induced phase separation in polar active liquids, *Physical Review X* **9**, 031043 (2019).
- [65] S. Verma, G. Novati, and P. Koumoutsakos, Efficient collective swimming by harnessing vortices through deep reinforcement learning, *Proceedings of the National Academy of Sciences* **115**, 5849–5854 (2018).
- [66] D. Waelchli, P. Weber, and P. Koumoutsakos, Discovering individual rewards in collective behavior through inverse multi-agent reinforcement learning (2023), arXiv:2305.10548.
- [67] S. Colabrese, K. Gustavsson, A. Celani, and L. Biferale, Flow navigation by smart microswimmers via reinforcement learning, *Physical Review Letters* **118**, 158004 (2017).
- [68] M. Durve, L. Piro, M. Cencini, L. Biferale, and A. Celani, Collective olfactory search in a turbulent environment, *Physical Review E* **102**, 012402 (2020).
- [69] T. C. Schelling, Dynamic models of segregation, *The Journal of Mathematical Sociology* **1**, 143 (1971).
- [70] T. C. Schelling, *Micromotives and macrobehaviour*. (W.W.Norton, 1980) p. 256.
- [71] D. Card, A. Mas, and J. Rothstein, Tipping and the dynamics of segregation, *Quarterly Journal of Economics* **123**, 177 (2008).
- [72] D. Vinković and A. Kirman, A physical analogue of the schelling model, *Proceedings of the National Academy of Sciences* **103**, 19261 (2006).
- [73] S. Grauwijn, F. Goffette-Nagot, and P. Jensen, Dynamic models of residential segregation: An analytical solution, *Journal of Public Economics* **96**, 124 (2012).
- [74] J. Zhang, Tipping and residential segregation: A unified schelling model, *Journal of Regional Science* **51**, 167

- (2011).
- [75] W. A. V. Clark and M. Fossett, Understanding the social context of the schelling segregation model, *Proceedings of the National Academy of Sciences* **105**, 4109 (2008).
- [76] M. Fossett, Ethnic preferences, social distance dynamics, and residential segregation: Theoretical explorations using simulation analysis*, *The Journal of Mathematical Sociology* **30**, 185 (2006).
- [77] L. Gauvin, J. Vannimenus, and J.-P. Nadal, Phase diagram of a schelling segregation model, *The European Physical Journal B* **70**, 293 (2009).
- [78] R. Zakine, J. Garnier-Brun, A.-C. Becharat, and M. Benzaquen, Socioeconomic agents as active matter in nonequilibrium sakoda-schelling models, arXiv 10.48550/arXiv.2307.14270 (2023), 2307.14270.
- [79] M. Starnini, A. Baronchelli, and R. Pastor-Satorras, Modeling human dynamics of face-to-face interaction networks, *Physical Review Letters* **110**, 168701 (2013).
- [80] S. H. Choi, V. D. Rao, T. Gernat, A. R. Hamilton, G. E. Robinson, and N. Goldenfeld, Individual variations lead to universal and cross-species patterns of social behavior, *Proceedings of the National Academy of Sciences* **117**, 31754 (2020).
- [81] Turing, Alan, The chemical basis of morphogenesis, *Philosophical Transactions of the Royal Society of London. Series B, Biological Sciences* **237**, 37 (1952).
- [82] D. Gilmour, M. Rembold, and M. Leptin, From morphogen to morphogenesis and back, *Nature* **541**, 311–320 (2017).
- [83] M. Lefebvre, J. Colen, N. Claussen, F. Brauns, M. Raich, N. Mitchell, M. Fruchart, V. Vitelli, and S. J. Streichan, *Learning a conserved mechanism for early neuroectoderm morphogenesis* (2023).
- [84] J. V. Neumann and O. Morgenstern, *Theory of Games and Economic Behavior* (Princeton University Press, 2007) p. 776.
- [85] M. J. Osborne and A. Rubinstein, *A course in game theory*, 12th ed. (MIT Press, Cambridge, Mass. [u.a.], 2006) literaturverz. S. [321] - 339.
- [86] C. Z. Charles, The dynamics of racial residential segregation, *Annual Review of Sociology* **29**, 167 (2003).
- [87] S. Manson, J. Schroeder, D. Van Riper, T. Kugler, and S. Ruggles, *National historical geographic information system: Version 17.0* (2022).
- [88] D. R. Williams and C. Collins, Racial residential segregation: A fundamental cause of racial disparities in health, *Public Health Reports* **116**, 404 (2001).
- [89] D. Pager and H. Shepherd, The sociology of discrimination: Racial discrimination in employment, housing, credit, and consumer markets, *Annual Review of Sociology* **34**, 181 (2008).
- [90] S. F. Reardon and A. Owens, 60 years after brown: Trends and consequences of school segregation, *Annual Review of Sociology* **40**, 199 (2014).
- [91] D. Alexander and J. Currie, Is it who you are or where you live? residential segregation and racial gaps in childhood asthma, *Journal of Health Economics* **55**, 186 (2017).
- [92] W. E. B. Du Bois, *The souls of black folk*, edited by I. X. Kendi and M. M. Elbert, Penguin classics (Penguin Books, New York, 2018).
- [93] D. S. Massey, American apartheid: Segregation and the making of the underclass, *American Journal of Sociology* **96**, 329 (1990).
- [94] P. A. Jargowsky, *Poverty and Place* (Russell Sage Foundation, New York, 1998) description based upon print version of record.
- [95] K. E. Taeuber and A. F. Taeuber, *Residential segregation and neighborhood change* (Transaction Publishers, 2008).
- [96] M. S. Schmitt, M. Koch-Janusz, M. Fruchart, D. S. Seara, and V. Vitelli, Information theory for model reduction in stochastic dynamical systems (2023), arXiv:2312.06608.
- [97] M. S. Schmitt, J. Colen, S. Sala, J. Devany, S. Seetharaman, M. L. Gardel, P. W. Oakes, and V. Vitelli, Zyxin is all you need: Machine learning adherent cell mechanics (2023), arxiv:2303.00176 [cond-mat, physics:physics].
- [98] O. D. Duncan and B. Duncan, A methodological analysis of segregation indexes, *American Sociological Review* **20**, 210 (1955).
- [99] S. F. Reardon and D. O’Sullivan, Measures of spatial segregation, *Sociological Methodology* **34**, 121 (2004).
- [100] J. R. Logan, B. J. Stults, and R. Farley, Segregation of minorities in the metropolis: two decades of change, *Demography* **41**, 1 (2004).
- [101] B. Elbers, Trends in u.s. residential racial segregation, 1990 to 2020, *Socius: Sociological Research for a Dynamic World* **7**, 237802312110539 (2021).
- [102] J. Hwang and T. W. McDaniel, Racialized reshuffling: Urban change and the persistence of segregation in the twenty-first century, *Annual Review of Sociology* **48**, 397 (2022).
- [103] There are some differences between locations. For example, segregation in Los Angeles County, California and Harris County, Texas show the fastest decreases, which may be attributed to a rise in Hispanic populations [102].
- [104] US Census Bureau, Calculating migration expectancy using acs data, <https://www.census.gov/topics/population/migration/guidance/calculating-migration-expectancy.html>, accessed: 2023-08-01.
- [105] S. Gandon, T. Day, C. J. E. Metcalf, and B. T. Grenfell, Forecasting epidemiological and evolutionary dynamics of infectious diseases, *Trends in Ecology & Evolution* **31**, 776 (2016).
- [106] J. Marchi, M. Lässig, A. M. Walczak, and T. Mora, Antigenic waves of virus-immune coevolution, *Proceedings of the National Academy of Sciences* **118**, 10.1073/pnas.2103398118 (2021).
- [107] K. Simonyan, A. Vedaldi, and A. Zisserman, Deep inside convolutional networks: Visualising image classification models and saliency maps (2014), arXiv:1312.6034 [cs.CV].
- [108] F. J. Dyson, Existence of a phase-transition in a one-dimensional ising ferromagnet, *Communications in Mathematical Physics* **12**, 91 (1969).
- [109] R. Farley, C. Steeh, T. Jackson, M. Krysan, and K. Reeves, Continued racial residential segregation in detroit: "chocolate city, vanilla suburbs" revisited, *Journal of Housing Research* **4**, 1 (1993).
- [110] W. A. V. Clark, Ethnic preferences and ethnic perceptions in multi-ethnic settings, *Urban Geography* **23**, 237 (2002).
- [111] L. Bobo and C. L. Zubrinsky, Attitudes on residential integration: Perceived status differences, mere in-group preference, or racial prejudice?, *Social Forces* **74**, 883 (1996).
- [112] N. D. Daw, J. P. O’Doherty, P. Dayan, B. Seymour, and R. J. Dolan, Cortical substrates for exploratory decisions

- in humans, *Nature* **441**, 876 (2006).
- [113] J. I. Gold and M. N. Shadlen, The neural basis of decision making, *Annual Review of Neuroscience* **30**, 535 (2007).
- [114] R. Ratcliff and G. McKoon, The diffusion decision model: Theory and data for two-choice decision tasks, *Neural Computation* **20**, 873 (2008).
- [115] R. Ratcliff, P. L. Smith, S. D. Brown, and G. McKoon, Diffusion decision model: Current issues and history, *Trends in Cognitive Sciences* **20**, 260 (2016).
- [116] E. Ben-Naim, P. Krapivsky, and S. Redner, Bifurcations and patterns in compromise processes, *Physica D: Nonlinear Phenomena* **183**, 190–204 (2003).
- [117] P. L. Krapivsky, *A kinetic view of statistical physics*, edited by S. Redner and E. Ben-Naim (Cambridge University Press, Cambridge, 2013) title from publisher’s bibliographic system (viewed on 05 Oct 2015).
- [118] S. Redner, Reality-inspired voter models: A mini-review, *Comptes Rendus Physique* **20**, 275–292 (2019).
- [119] P. A. Samuelson, A note on measurement of utility, *The Review of Economic Studies* **4**, 155 (1937).
- [120] J. Hofbauer and K. Sigmund, *Evolutionary Games and Population Dynamics* (Cambridge University Press, 1998).
- [121] J.-P. Bouchaud, Crises and collective socio-economic phenomena: Simple models and challenges, *Journal of Statistical Physics* **151**, 567 (2013).
- [122] R. Farley, H. Schuman, S. Bianchi, D. Colasanto, and S. Hatchett, ”chocolate city, vanilla suburbs”: Will the trend toward racially separate communities continue?, *Social Science Research* **7**, 319 (1978).
- [123] W. Clark, Residential preferences and neighborhood racial segregation: A test of the schelling segregation model, *Demography* **28**, 1 (1991).
- [124] E. F. Keller and L. A. Segel, Model for chemotaxis, *Journal of Theoretical Biology* **30**, 225 (1971).
- [125] M. Vergassola, E. Villermanx, and B. I. Shraiman, ‘infotaxis’ as a strategy for searching without gradients, *Nature* **445**, 406–409 (2007).
- [126] J. W. Cahn and J. E. Hilliard, Free energy of a nonuniform system. i. interfacial free energy, *The Journal of Chemical Physics* **28**, 258 (1958).
- [127] P. C. Hohenberg and B. I. Halperin, Theory of dynamic critical phenomena, *Reviews of Modern Physics* **49**, 435 (1977).
- [128] D. Lauffenburger, C. R. Kennedy, and R. Aris, Traveling bands of chemotactic bacteria in the context of population growth, *Bulletin of Mathematical Biology* **46**, 19 (1984).
- [129] C. M. Taylor and A. Hastings, Allee effects in biological invasions, *Ecology Letters* **8**, 895 (2005).
- [130] O. Hallatschek and D. R. Nelson, Gene surfing in expanding populations, *Theoretical Population Biology* **73**, 158 (2008).
- [131] K. S. Korolev, M. Avlund, O. Hallatschek, and D. R. Nelson, Genetic demixing and evolution in linear stepping stone models, *Reviews of Modern Physics* **82**, 1691 (2010).
- [132] J. Saragosti, V. Calvez, N. Bournaveas, B. Perthame, A. Buguin, and P. Silberzan, Directional persistence of chemotactic bacteria in a traveling concentration wave, *Proceedings of the National Academy of Sciences* **108**, 16235 (2011).
- [133] K. S. Korolev, M. J. I. Müller, N. Karahan, A. W. Murray, O. Hallatschek, and D. R. Nelson, Selective sweeps in growing microbial colonies, *Physical Biology* **9**, 026008 (2012).
- [134] S. Pigolotti, R. Benzi, P. Perlekar, M. Jensen, F. Toschi, and D. Nelson, Growth, competition and cooperation in spatial population genetics, *Theoretical Population Biology* **84**, 72 (2013).
- [135] W. Liu, J. Cremer, D. Li, T. Hwa, and C. Liu, An evolutionarily stable strategy to colonize spatially extended habitats, *Nature* **575**, 664 (2019).
- [136] S. Gude, E. Pınar, K. M. Taute, A.-B. Seinen, T. S. Shimizu, and S. J. Tans, Bacterial coexistence driven by motility and spatial competition, *Nature* **578**, 588 (2020).
- [137] D. R. Nelson and N. M. Shnerb, Non-hermitian localization and population biology, *Physical Review E* **58**, 1383–1403 (1998).
- [138] M. J. I. Müller, B. I. Neugeboren, D. R. Nelson, and A. W. Murray, Genetic drift opposes mutualism during spatial population expansion, *Proceedings of the National Academy of Sciences* **111**, 1037–1042 (2014).
- [139] P. Perlekar, R. Benzi, D. R. Nelson, and F. Toschi, Population dynamics at high reynolds number, *Physical Review Letters* **105**, 144501 (2010).
- [140] S. Pigolotti, R. Benzi, M. H. Jensen, and D. R. Nelson, Population genetics in compressible flows, *Physical Review Letters* **108**, 128102 (2012).
- [141] S. Atis, B. T. Weinstein, A. W. Murray, and D. R. Nelson, Microbial range expansions on liquid substrates, *Physical Review X* **9**, 021058 (2019).
- [142] J. F. Crow and M. Kimura, *An Introduction to Population Genetics Theory* (Blackburn Press, 1970) p. 608.
- [143] M. Kimura, *The neutral theory of molecular evolution* (Cambridge University Press, 1983).
- [144] L. S. Tsimring, H. Levine, and D. A. Kessler, RNA virus evolution via a fitness-space model, *Physical Review Letters* **76**, 4440 (1996).
- [145] V. Mustonen and M. Lässig, From fitness landscapes to seascapes: non-equilibrium dynamics of selection and adaptation, *Trends in Genetics* **25**, 111 (2009).
- [146] J. Adler, Chemotaxis in bacteria, *Annual Review of Biochemistry* **44**, 341 (1975).
- [147] H. C. Berg, Chemotaxis in bacteria, *Annual Review of Biophysics and Bioengineering* **4**, 119 (1975).
- [148] M. Fruchart, R. Hanai, P. B. Littlewood, and V. Vitelli, Non-reciprocal phase transitions, *Nature* **592**, 363 (2021).
- [149] Z. You, A. Baskaran, and M. C. Marchetti, Nonreciprocity as a generic route to traveling states, *Proceedings of the National Academy of Sciences* **117**, 19767 (2020).
- [150] S. Saha, J. Agudo-Canalejo, and R. Golestanian, Scalar Active Mixtures: The Nonreciprocal Cahn-Hilliard Model, *Physical Review X* **10**, 041009 (2020).
- [151] A. V. Ivlev, J. Bartnick, M. Heinen, C.-R. Du, V. Nosenko, and H. Löwen, Statistical mechanics where newton’s third law is broken, *Physical Review X* **5**, 011035 (2015).
- [152] C. Hargus, J. M. Epstein, and K. K. Mandadapu, Odd diffusivity of chiral random motion, *Physical Review Letters* **127**, 178001 (2021).
- [153] Y. Baek, A. P. Solon, X. Xu, N. Nikola, and Y. Kafri, Generic long-range interactions between passive bodies in an active fluid, *Physical Review Letters* **120**, 058002 (2018).
- [154] T. Frohoff-Hülsmann, J. Wrembel, and U. Thiele, Sup-

- pression of coarsening and emergence of oscillatory behavior in a cahn-hilliard model with nonvariational coupling, *Physical Review E* **103**, 042602 (2021).
- [155] F. Brauns and M. C. Marchetti, Non-reciprocal pattern formation of conserved fields, arXiv (2023), arXiv:2306.08868.
- [156] A. Dinelli, J. O’Byrne, A. Curatolo, Y. Zhao, P. Sollich, and J. Tailleur, Non-reciprocity across scales in active mixtures, arXiv (2022), arXiv:2203.07757.
- [157] C. Scheibner, A. Souslov, D. Banerjee, P. Surówka, W. T. M. Irvine, and V. Vitelli, Odd elasticity, *Nature Physics* **16**, 475 (2020).
- [158] M. Fruchart, C. Scheibner, and V. Vitelli, Odd viscosity and odd elasticity, *Annual Review of Condensed Matter Physics* **14**, 471 (2023).
- [159] J. P. Banerjee, R. Mandal, D. S. Banerjee, S. Thutupalli, and M. Rao, Unjamming and emergent nonreciprocity in active ploughing through a compressible viscoelastic fluid, *Nature Communications* **13**, 10.1038/s41467-022-31984-z (2022).
- [160] R. Lemoy, E. Bertin, and P. Jensen, Socio-economic utility and chemical potential, *EPL (Europhysics Letters)* **93**, 38002 (2011).
- [161] N. C. Keim, J. D. Paulsen, Z. Zeravcic, S. Sastry, and S. R. Nagel, Memory formation in matter, *Reviews of Modern Physics* **91**, 035002 (2019).
- [162] S. G. Meyer, *As long as they don’t move next door: Segregation and racial conflict in American neighborhoods* (Rowman & Littlefield, 2000).
- [163] J. Yinger, Evidence on discrimination in consumer markets, *Journal of Economic Perspectives* **12**, 23 (1998).
- [164] D. S. Massey and G. Lundy, Use of black english and racial discrimination in urban housing markets: New methods and findings, *Urban Affairs Review* **36**, 452 (2001).
- [165] G. Galster, Racial discrimination in housing markets during the 1980s: A review of the audit evidence, *Journal of Planning Education and Research* **9**, 165 (1990).
- [166] C. Z. Charles, Neighborhood racial-composition preferences: Evidence from a multiethnic metropolis, *Social Problems* **47**, 379 (2000).
- [167] C. L. Zubrinsky and L. Bobo, Prismatic metropolis: Race and residential segregation in the city of the angels, *Social Science Research* **25**, 335 (1996).
- [168] B. Kerr, M. A. Riley, M. W. Feldman, and B. J. M. Bohannan, Local dispersal promotes biodiversity in a real-life game of rock–paper–scissors, *Nature* **418**, 171 (2002).
- [169] G. J. Velicer, Social strife in the microbial world, *Trends in Microbiology* **11**, 330 (2003).
- [170] M. E. Hibbing, C. Fuqua, M. R. Parsek, and S. B. Peterson, Bacterial competition: surviving and thriving in the microbial jungle, *Nature Reviews Microbiology* **8**, 15 (2009).
- [171] E. D. Kelsic, J. Zhao, K. Vetsigian, and R. Kishony, Counteraction of antibiotic production and degradation stabilizes microbial communities, *Nature* **521**, 516 (2015).
- [172] J. D. Van Dyken, M. J. Müller, K. M. Mack, and M. M. Desai, Spatial Population Expansion Promotes the Evolution of Cooperation in an Experimental Prisoner’s Dilemma, *Current Biology* **23**, 919 (2013).
- [173] C. Ratzke, J. Barrere, and J. Gore, Strength of species interactions determines biodiversity and stability in microbial communities, *Nature Ecology & Evolution* **4**, 376 (2020).
- [174] M. B. Miller and B. L. Bassler, Quorum sensing in bacteria, *Annual Review of Microbiology* **55**, 165–199 (2001).
- [175] C. M. Waters and B. L. Bassler, Quorum sensing: Cell-to-cell communication in bacteria, *Annual Review of Cell and Developmental Biology* **21**, 319 (2005).
- [176] S. Chatterjee, R. A. da Silveira, and Y. Kafri, Chemotaxis when bacteria remember: Drift versus diffusion, *PLoS Computational Biology* **7**, e1002283 (2011).
- [177] Y. Kafri and R. A. da Silveira, Steady-state chemotaxis in escherichia coli, *Physical Review Letters* **100**, 238101 (2008).
- [178] D. R. Mills, R. L. Peterson, and S. Spiegelman, An extracellular darwinian experiment with a self-duplicating nucleic acid molecule., *Proceedings of the National Academy of Sciences* **58**, 217 (1967).
- [179] G. P. Smith, Filamentous fusion phage: Novel expression vectors that display cloned antigens on the virion surface, *Science* **228**, 1315 (1985).
- [180] K. Chen and F. H. Arnold, Enzyme engineering for non-aqueous solvents: Random mutagenesis to enhance activity of subtilisin e in polar organic media, *Bio/Technology* **9**, 1073 (1991).
- [181] N. Q. Balaban, J. Merrin, R. Chait, L. Kowalik, and S. Leibler, Bacterial persistence as a phenotypic switch, *Science* **305**, 1622 (2004).
- [182] E. Kussell and S. Leibler, Phenotypic diversity, population growth, and information in fluctuating environments, *Science* **309**, 2075 (2005).
- [183] A. Murugan, K. Husain, M. J. Rust, C. Hepler, J. Bass, J. M. J. Pietsch, P. S. Swain, S. G. Jena, J. E. Toettcher, A. K. Chakraborty, K. G. Sprenger, T. Mora, A. M. Walczak, O. Rivoire, S. Wang, K. B. Wood, A. Skanata, E. Kussell, R. Ranganathan, H.-Y. Shih, and N. Goldenfeld, Roadmap on biology in time varying environments, *Physical Biology* **18**, 041502 (2021).
- [184] M. Lässig, V. Mustonen, and A. M. Walczak, Predicting evolution, *Nature Ecology and Evolution* **1**, 10.1038/s41559-017-0077 (2017).
- [185] R. Farley, E. L. Fielding, and M. Krysan, The residential preferences of blacks and whites: A four-metropolis analysis, *Housing Policy Debate* **8**, 763 (1997).
- [186] Z. Liu, H. Mao, C.-Y. Wu, C. Feichtenhofer, T. Darrell, and S. Xie, *A convnet for the 2020s* (2022).
- [187] E. Bertin, *Statistical Physics of Complex Systems A Concise Introduction* (Springer International Publishing AG, 2021) p. 291.
- [188] R. J. Glauber, Time-dependent statistics of the ising model, *Journal of Mathematical Physics* **4**, 294 (1963).
- [189] H. Eyring, The activated complex in chemical reactions, *The Journal of Chemical Physics* **3**, 107 (1935).
- [190] M. R. Evans and T. Hanney, Nonequilibrium statistical mechanics of the zero-range process and related models, *Journal of Physics A: Mathematical and General* **38**, R195 (2005).
- [191] T. Frohoff-Hülsmann, M. P. Holl, E. Knobloch, S. V. Gurevich, and U. Thiele, Stationary broken parity states in active matter models, *Physical Review E* **107**, 064210 (2023).

Supplementary Materials

CONTENTS

I. The sociohydrodynamic pipeline	3
A. Identifying collective variables in social behavior	3
B. Assessing predictability and locality with neural networks	3
C. Extracting utility functions from social surveys.	6
D. Constructing a hydrodynamic theory	6
II. The sociohydrodynamic model	7
A. A phase diagram for social behavior	7
B. Emergent history-dependence of desegregation	8
III. Discussion and outlook	9
IV. Methods	11
A. US Census Data.	11
B. Segregation Indices	11
C. Sociohydrodynamic diffusion matrix.	11
D. Simulation methods.	11
E. Linear utility functions.	11
F. Empirical utility functions.	11
G. Assessing locality via neural networks	11
References	13
V. Supplementary Figures	19
VI. Supplementary Notes	23
A. US Census Data	23
B. Segregation indices	23
C. Survey questions	24
1. Farley, 1993 [109]	24
2. Clark, 2002 [110]	25
D. Assessing locality via neural networks	25
1. Neural network architecture and training	25
2. Post-processing and saliency analysis	26
E. Agent-based segregation dynamics	27
1. The utility function	27
2. The transition rates	27
F. Derivation of sociohydrodynamic equations	28
G. The potential function	32
1. Demonstration of $L(\phi)$ as a potential function	34
2. Relaxational dynamics	35
H. Linear Stability Analysis	36
I. Linear utilities	37
1. Phase space criteria.	38
J. Empirical utility functions	38
K. Population dynamics	38

V. SUPPLEMENTARY FIGURES

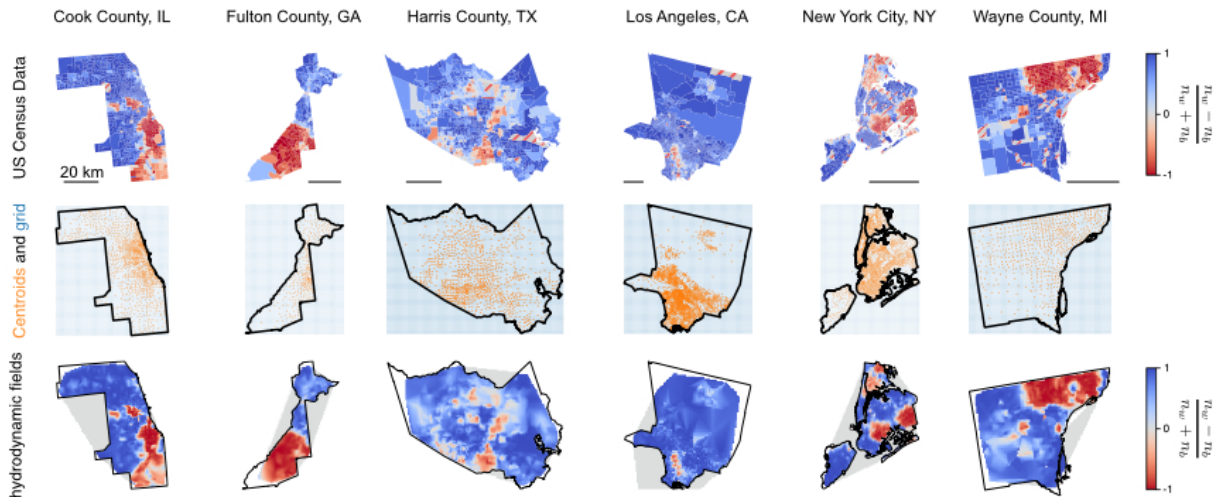


FIG. 7. **Census data interpolation.** Top row shows relative proportions of White and Black residents in 2020 census data, measured as $(n_w - n_b)/(n_w + n_b)$. Middle row shows census tract centroids (in orange) and the corresponding grid on which the fields are interpolated (in blue). Bottom show the resulting interpolated fields. The interpolation occurs over convex hull of the centroids, which is why some regions are white. Gray areas outside of the black boundaries are neglected to the masking discussed in the section above.

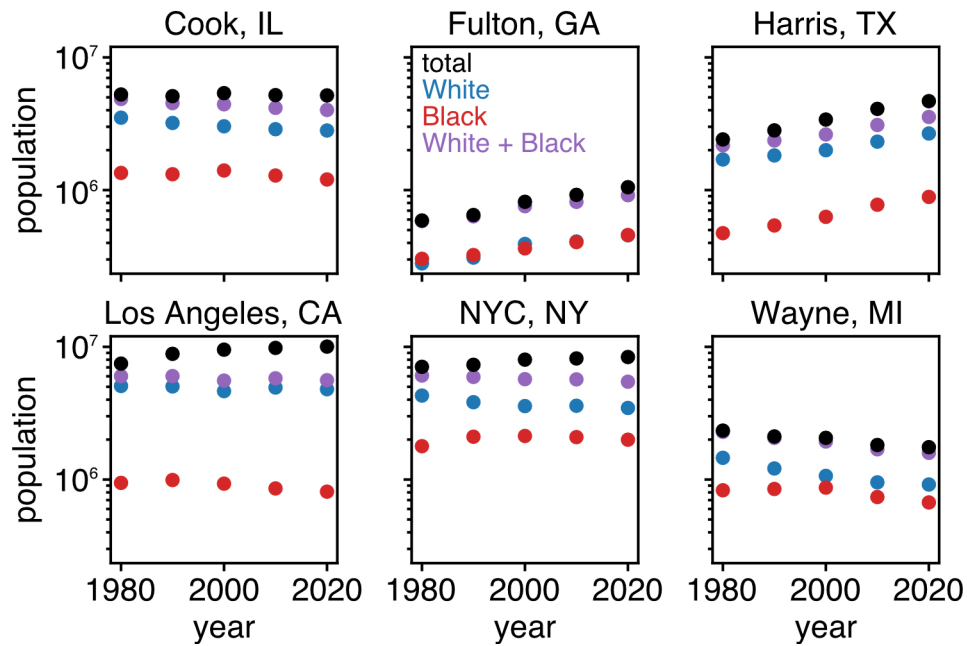


FIG. 8. **Total population numbers in the six areas studied in the main text.** Population numbers are measured from decennial US Census data from 1980-2020, shown on a semilog axis. Total, White, Black, and White + Black populations in black, blue, red, and purple, respectively. The growing gap between the total and White + Black population numbers indicate an increasing proportion of other races in those areas, predominantly Hispanic populations. The populations change roughly linearly on the semilog axis, reflecting a roughly exponential increase in population.

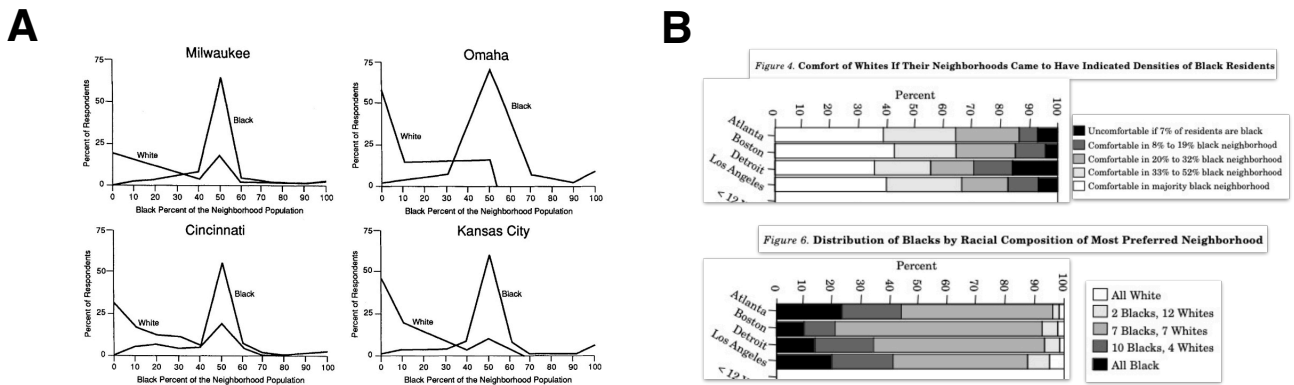


FIG. 9. **Survey results for neighborhood preferences.** (A) Reproduction of Fig.4 of Ref. [123]. Residents across all cities were asked to “Now suppose you have been looking for a house or apartment and have found a nice place you can afford. It could be located in neighborhoods with different racial groups. What mixture of people would you prefer? Would you prefer a neighborhood that is... (combinations of 100% white, 90% white and 10% black, and so on through 100% black were read to respondents)”. (B) Reproduces portions of Figs 4 & 6 from Ref. [185], with the corresponding questions written on top of each bar plot. Both cases show the generic features found in Fig. 1C, which itself reproduced data from Ref. [109] – neighborhood preferences of White respondents is monotonically decreasing with the proportion of Black residents, while Black respondents indicate a preference for mixed neighborhoods.

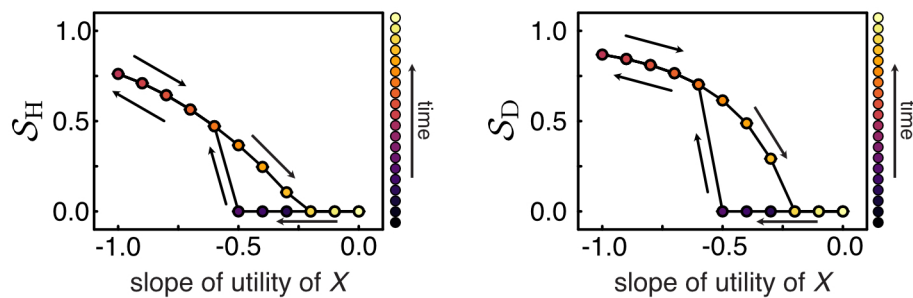


FIG. 10. **Annealing data for different segregation indices.** Left shows same data as in Fig. 6 in the main text, the entropy index S_H during the annealing process. Right shows the dissimilarity index, S_D for the same set of data.

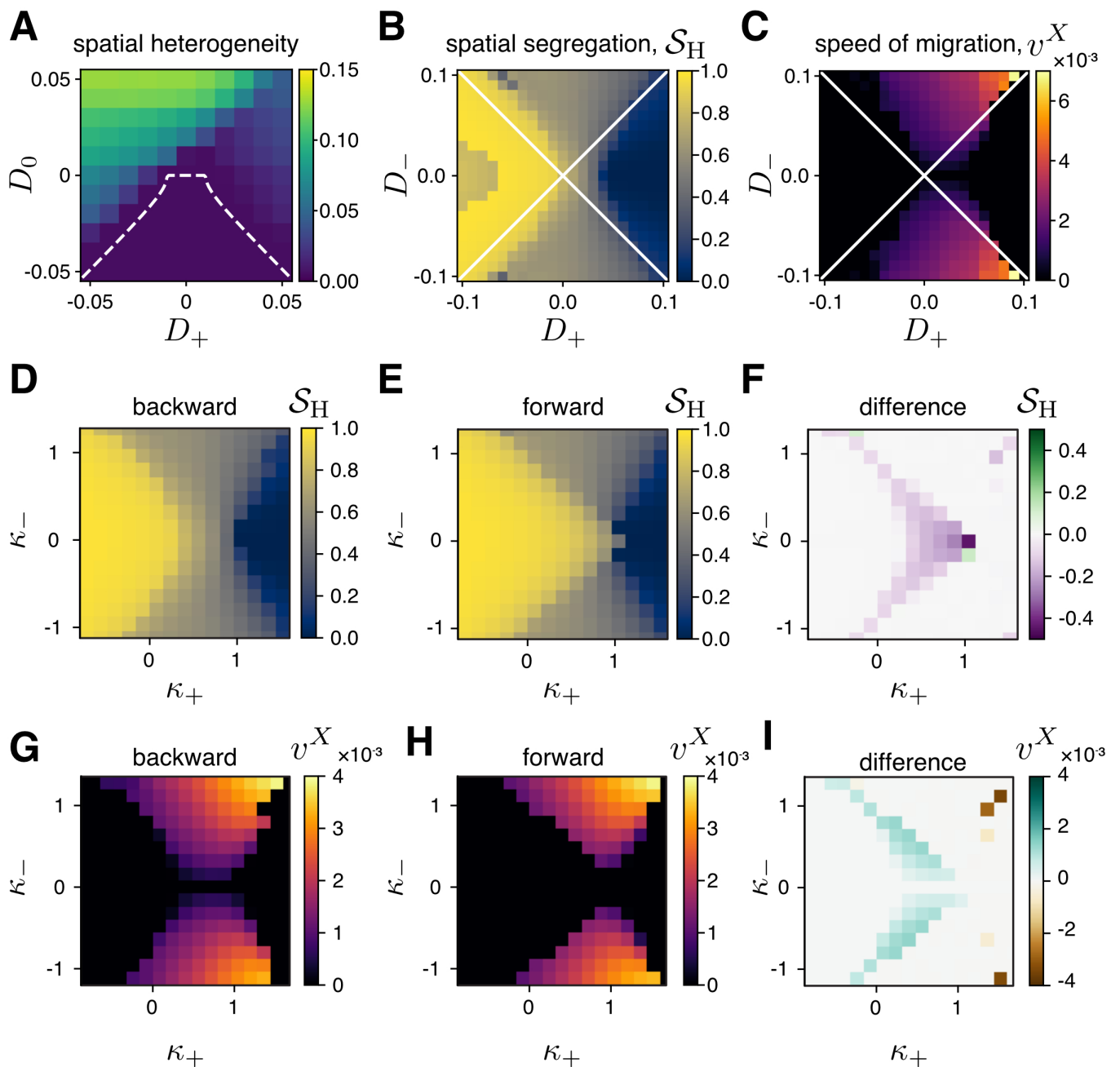


FIG. 11. **Amplitude, segregation, and velocity.** (A) Amplitude of patterns measured using Eq. 94 in the (D_+, D_0) plane for $D_- = 0.01$. (B) Shows the quantification of the segregation using Eq. 13. (C) migration speed of the pattern as defined in (95). All these cases begin with uniform initial conditions. (D-F) Segregation index for forward pass (D), backward pass (E), and their difference (F) using annealing protocol described in Sec. VII, starting from a maximum $\kappa_+ = 1.52$ and a minimum $\kappa_+ = -0.88$, with a step of $\Delta\kappa_+ = 0.16$. (G-I) Wave velocity for forward pass (G), backward pass (H), and their difference (I) using annealing protocol described in Sec. VII, starting from a maximum $\kappa_+ = 1.52$ and a minimum $\kappa_+ = -0.88$, with a step of $\Delta\kappa_+ = 0.16$.

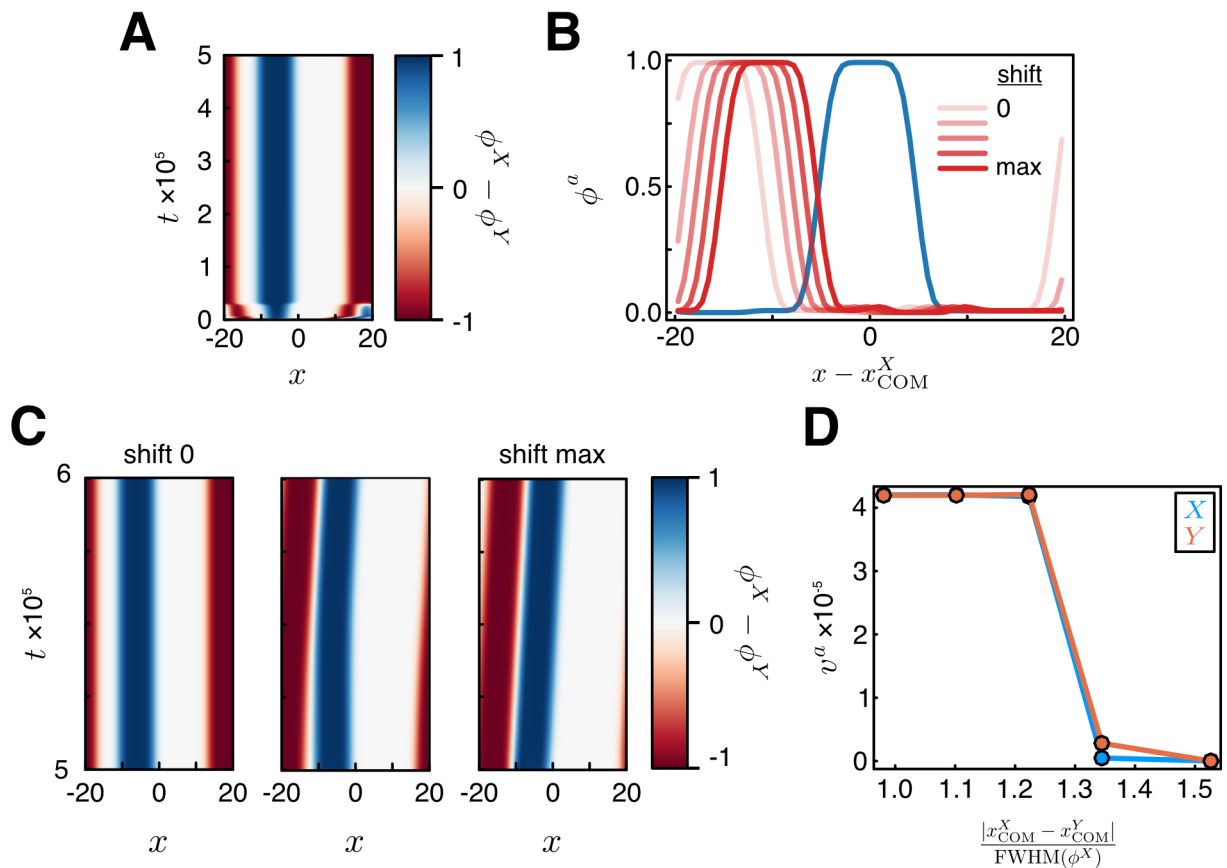


FIG. 12. **Migration speed depends on overlap between populations.** (A) Result of simulation using linear utilities, $\kappa_+ = 0.5$, $\kappa_- = 0.2$. The wave velocity after $t = t_f = 5 \times 10^5$ is zero. (B) Illustration of “shifting” the final distribution, $\phi^Y(t_f)$ (red). Shifts are done in units of the lattice spacing, $\Delta x = 0.625$, with a maximum shift of $10\Delta x$. (C) Results of restarting simulations after shifting ϕ^Y by different amounts. (D) Measurement of wave velocity after $t = 10^5$ of restarted dynamics as a function of the shift, showing that the distributions find a unique velocity once they overlap enough.

Region	ℓ (km)
Cook County, IL	1.37
Fulton County, GA	2.78
Harris County, TX	2.58
Los Angeles County, CA	2.31
New York City, NY	0.60
Wayne County, MI	1.60

TABLE I. Median census tract size for regions studied. Median is taken over all census tracts from 1980-2020.

VI. SUPPLEMENTARY NOTES

A. US Census Data

The US population data are decennial census data at the census tract level for decades 1980-2010 [87]. The 2020 data set was obtained from the 2016-2020 American Community survey. When possible, populations labeled as “White” or “Black” were taken to be non-Hispanic White and non-Hispanic Black. We further used GIS data to give proper physical coordinates to the population data using the 2008 TIGER/Line GIS for years 1980-2000, and the 2020 TIGER/Line GIS for years 2010 and 2020.

To coarse-grain and analyze the population data, we perform an interpolation for each studied region separately. After reading the GIS shapefile using the GeoPandas, we use the GeoPandas ‘centroid’ function to find a point internal to the census tract. We then assign the value of each population within that census tract to the centroid. Using the full range of the given region as a bounding box, we create a regular grid and use the ‘scipy.interpolate.griddata’ method. Next, we mask the resulting interpolated data using the boundaries of the region. In this way, we circumnavigate the difficulties in measuring spatiotemporal characteristics across censuses that come from small changes to the definitions of census tracts across time. See Supplementary Figure 1.

We measure the correlation length of the fluctuations of the two populations using standard Fourier Transform methods. Specifically, for each population we calculate $\delta n^a(x, t) = n^a(x, t) - \langle n^a \rangle$, where the average is taken over space and time. We then calculate the spatial Fourier transform, $\mathcal{F}_q [\delta n^a(x, t)] = \delta n^a(q, t)$, and calculate the autocorrelation function as

$$C_{aa}(x) = \mathcal{F}_q^{-1} \left[\langle |\delta n(q, t)|^2 \rangle_t \right]. \quad (12)$$

Across the regions shown in Fig. 7, we measure a mean correlation length for White and Black populations to be $\langle \xi_w \rangle = 11.7 \pm 4.2$ km and $\langle \xi_b \rangle = 7.9 \pm 3.9$ km. We also note that the fluctuations measured are within $\pm \langle n \rangle$, although there is a slight trend downwards (upwards) for the White (Black) populations.

The typical census tract sizes for the different areas studied are found using the areas of all census tracts, A_i , and finding median $(\sqrt{A_i})$.

B. Segregation indices

In order to quantify both the measured distribution of human populations as well as our simulations, we utilize segregation indices. Mathematically, a segregation index is measured by a functional \mathcal{S} that takes the distribution of ≥ 2 populations to generate a scalar measure of how spatially separated the populations [99]. We will normalize our indices such that 0 means the system is perfectly integrated, and 1 means the system is completely segregated. We stress that “integration” does not mean that a location has 50 – 50 representation of each group, but rather that proportion of each group present locally is equal to the proportion of each group present globally. For example, if a region comprises 70% White residents and 30% Black residents, the region is integrated if each location within the region also comprises 70% White residents and 30% Black residents.

Our notation is defined in Table II and largely follows [99]. We call a “region” the full geographic area we consider (e.g. Cook County, New York City), and a *neighborhood* a small area within the region (e.g. an individual census tract). The entropy index used in the main text, which we will denote here as \mathcal{S}_H , is a weighted mean of an entropy

Variable	Definition
m	index of subgroup
i	index of neighborhood
t_i^m	total number of group m in neighborhood i
$t^m = \sum_i t_i^m$	total number of m in region
$t_i = \sum_m t_i^m$	total number of people in neighborhood
$T = \sum_{m,i} t_i^m$	total number of people in region
$p_i^m = t_i^m / t_i$	proportion of residents in neighborhood i of type m
$p^m = t^m / T$	proportion of residents in region of type m

TABLE II. Notation used for defining and calculating segregation indices.

index field h_i , defined as

$$h_i = \frac{\sum_m p_i^m \ln \left(\frac{p_i^m}{p^m} \right)}{-\sum_m p_m \ln p_m} \quad (13a)$$

$$\mathcal{S}_h[p_i^m] = \frac{1}{T} \sum_i t_i h_i. \quad (13b)$$

The spatial maps of segregation in Figs. 1&3 show h_i , which measures the Kullback-Leibler divergence between the local composition distribution p_i^m to the region's composition distribution p_m , normalized by the Shannon entropy of the region's composition. The entropy index is the population-weighted mean of h_i .

This choice of index is not unique. Another common index used in the sociology literature is the so-called ‘‘dissimilarity index’’, which we will denote as \mathcal{S}_D . Like \mathcal{S}_H , it measures how different local compositions are compared to the global composition. Again, it is given by a weighted mean of a field, d_i , defined for binary populations as

$$d_i = \frac{1}{2} \frac{|p_i^m - p^m|}{p_m(1 - p_m)} \quad (14a)$$

$$\mathcal{S}_D = \frac{1}{T} \sum_i t_i d_i. \quad (14b)$$

We note that the binary population assumption ensures d_i is the same regardless of which subgroup m is chosen.

In Fig. 10, we reproduce the results from the annealing simulations shown in Fig. 3E along-side measurements using the dissimilarity index, illustrating that the two measurements give the same qualitative results.

C. Survey questions

In Fig. 4 of the main text, we show the results of surveys taken in Farley, 1993 [109] (Fig. 4A) and Clark, 2002 [110] (Fig. 4B). Here, we report the precise questions asked in each survey.

1. Farley, 1993 [109]

Surveyed Black respondents were given the following prompt (from Section ‘‘Residential Preferences of Blacks’’, bottom of page 20 in [109]):

We showed blacks five diagrams of neighborhoods (see figure 7). Each card pictured 15 homes with varying racial compositions ranging from all black to all white. Respondents were asked to imagine that they were searching for a home and found one they could afford. This home was shown as the center of each neighborhood. They were then asked to rank the neighborhoods from most to least attractive. The percent who said a specific neighborhood was their first or second choice is shown in figure 8.

The resulting data are reproduced by the red markers in Fig. 4A.

Surveyed White respondents were given the following prompt (from Section ‘‘Residential Preferences of Whites’’, bottom of page 23 in [109])

The residential preferences of whites were studied in a manner similar but not exactly identical to that used with blacks. Every white was presented with a series of diagrams showing neighborhoods with 15 homes (see figure 9). We asked them to imagine that they lived in an all-white neighborhood, a realistic assumption for most, and that the center home was theirs. They were then shown the second card, which indicated 1 home occupied by a black family and 14 by whites. Whites were asked how comfortable they would feel in that minimally integrated neighborhood. If they said "comfortable," they were shown cards with higher representations of blacks until they either said "uncomfortable" or came to the final card, which portrayed a majority-black neighborhood.

The resulting proportion of respondents indicating they were comfortable with each neighborhood are reproduced by the blue markers in Fig. 4A.

2. Clark, 2002 [110]

Surveyed Black respondents were asked (from page 243 of [110])

Now I would like you to imagine that you have been looking for a house and have found a nice house you can afford. This house could be located in several different types of neighborhoods as shown on these cards. (The cards show combinations of 15 own- and other-race houses indicated by stylized drawings.) Would you look through the cards and rearrange them so that the neighborhood that is most attractive to you is on top, the next most attractive second, and so on down the line with the least attractive neighborhood on the bottom.

The results for the proportion of respondents ranking a specific neighborhood as their first choice is reproduced by the red symbols in Fig. 4B.

Surveyed White respondents were asked (from page 243 of [110])

Now, I'd like you to imagine yourself in a different situation. Suppose you have been looking for a house and have found a nice one you can afford. This house could be located in several different types of neighborhoods, as shown on these cards (similar to those described above). Would you consider moving into any of these neighborhoods?

The results for the proportion of respondents indicating that they would move into a particular neighborhood is reproduced by the blue symbols in Fig. 4B.

D. Assessing locality via neural networks

We trained using decennial Census Data (1980-2020) from four counties: Cook IL, Harris TX, Fulton GA, and Los Angeles CA. While Fig. 6 also contains NYC NY and Wayne MI, we omitted them here due to the complexity posed by their geometry. For each county, we first downsampled the population data to a scale of 1 pixel = 1 km and performed Gaussian smoothing to soften sharp corners in the sampled areas. Next, we converted the raw populations into an occupation fraction ϕ by dividing the population at each pixel by the maximum total occupancy at that pixel over the entire time range. Each training example contained an input-output pair: the input was an image of occupation fractions for the county interpolated to a random time point $t_0 \in [1980, 2020]$, while the output was a second image of occupation fractions at some future time $t_0 + \Delta t$ where $\Delta t \in [0, 1]$. The machine learning model was tasked with predicting this future state $\vec{\phi}(t_0 + \Delta t)$ from the initial condition $\vec{\phi}(t_0)$.

1. Neural network architecture and training

We used a convolutional neural network to predict dynamics from the input data. The full architecture is outlined in Table III and implemented using the Pytorch library. Briefly, it contains two sequential modules of 8 convolutional blocks. The first computes latent features at the scale of the input data, while the second computes additional information using a downsampled representation of these latent features. As this second layer operates at a coarse-grained level, it can aggregate spatial information over a longer range. Throughout the network, we use ConvNext-style blocks [186].

This neural network processes a 2-channel image (ϕ^W, ϕ^B) and outputs another 2-channel image representing the predicted time derivative of the input $(\partial_t \phi^W, \partial_t \phi^B)$. We evaluated the quality of these predictions by integrating

Module	Size in	Size out	Details
Read-in	$2 \times H \times W$	$C \times H \times W$	1×ConvNext
CNN1	$C \times H \times W$	$C \times H \times W$	8×ConvNext
Downsample	$C \times H \times W$	$C \times H/4 \times W/4$	Strided Conv2d
CNN2	$C \times H/4 \times W/4$	$C \times H/4 \times W/4$	8×ConvNext
Upsample	$C \times H/4 \times W/4$	$C \times H \times W$	Interpolate
Skip		$2C \times H \times W$	Concat CNN1, CNN 2 outputs
Read-out	$2C \times H \times W$	$2 \times H \times W$	Conv2d

TABLE III. Neural network architecture. ConvNext layers are summarized in Table IV. We use a hidden size $C = 64$. The spatial dimensions H, W are determined by the input data.

Layer	Details	Channels	Kernel	Groups
Conv2d	Mix space	$N \rightarrow N$	7x7	N
LayerNorm				
Conv2d	Mix channels	$N \rightarrow 4N$	1x1	1
Sin	Activation			
Conv2d	Inverse bottleneck	$4N \rightarrow N$	1x1	1
Dropout	$p = 0.1$			

TABLE IV. ConvNext-style block architecture

them using a finite-element scheme that accounts for the geometry of the county’s boundary (see VID 2). To avoid accumulating errors when going from $\partial_t \vec{\phi}$ as an image (output by the NN) to $\partial_t \vec{\phi}$ on the mesh (used by the FEM method), we adapted the physical bottleneck approach introduced in [97]. During training, the network outputs are mapped to the county mesh and input to a FEM solver, implemented using the dolfin-adjoint library. The FEM solver integrates the predicted time derivatives on the county mesh over a period dt using a finite difference discretization. The network learns to minimize the loss

$$\mathcal{L} = \sum_b \left[\phi^b(t_0 + dt) - \hat{\phi}^b(t_0 + dt) \right]^2 \quad (15)$$

Here $\hat{\phi}_i$ is the predicted occupation fraction from the FEM solver. To train the neural network, we use the adjoint method (via dolfin-adjoint) to compute the gradient of this loss with respect to the network outputs $\partial \mathcal{L} / \partial (\partial_t \hat{\phi}^b)$. These gradients are passed to the Pytorch autograd library and used to update the weights of the neural network.

We train the model for 200 epochs with batch size 8. We use the Adam optimizer with learning rate $\lambda = 0.0003$ and exponential learning rate decay with $\gamma = 0.98$.

2. Post-processing and saliency analysis

After training, we use the network to predict population dynamics over the 40-year window spanned by the decennial Census data. Specifically, we solve the following initial value problem

$$\partial_t \vec{\phi}(t, \mathbf{r}) = f_{\text{Census}} \left[\vec{\phi}(t, \mathbf{r}) \right] \quad (16)$$

$$\vec{\phi}(1980, \mathbf{r}) = \text{US Census data from 1980} \quad (17)$$

To do this, we discretize the time derivative using finite differences as $\partial_t \vec{\phi} \approx (\vec{\phi}_{t+\Delta t} - \vec{\phi}_t) / \Delta t$ and iteratively compute $\vec{\phi}_{t+\Delta t}$ using a finite element approach implemented in Fenics. We used a time step $\Delta t = 0.1$ years and integrated the above equations as a closed loop for 40 years. Beyond the initial condition, the Census data was not seen by either the neural network or the FEM solver.

To assess locality in the predictions of the machine learning model, we computed output saliencies for the trained neural networks. Saliency is a measure of how much a model’s predictions depend on its inputs and is here defined as [107]

$$K^{ab}(\mathbf{r}_i, \mathbf{r}_j) = \frac{\partial(\partial_t \hat{\phi}^a(\mathbf{r}_i))}{\partial \phi^b(\mathbf{r}_j)} \quad (18)$$

Here a, b are population indices while i, j refer to spatial coordinates within each county. We compute $K^{ab}(\mathbf{r}_i, \mathbf{r}_j)$ from each input-output pair in each county dataset, for 100 randomly sampled output points \mathbf{r}_i and all input points \mathbf{r}_j . By azimuthally averaging, we aggregate this into a set of curves $K^{ab}(|\mathbf{r}_a - \mathbf{r}_b|)$ which are plotted in Figure 1.

E. Agent-based segregation dynamics

Here we describe the microscopic dynamics underlying our sociohydrodynamic equations. The set up amounts to a bounded-neighborhood variant of the Schelling model [9, 69, 73, 74, 78, 187].

We consider a system composed of two types of particles (agents), labeled by (X, Y) , distributed over a periodic lattice with M sites and lattice spacing l . Each lattice site can contain at most \mathcal{N} total particles. At a time t , lattice site i 's composition is given by the vector $\vec{n}_i(t) = (n_i^X(t), n_i^Y(t))$ giving the number of particles of both types at site i . The capacity constraint is $n_i^X(t) + n_i^Y(t) \leq \mathcal{N}$ for all i and all t . We use $\underline{n}(t) \equiv (\vec{n}_1(t), \vec{n}_2(t), \dots, \vec{n}_M(t))$ to indicate the full configuration of the system. Dividing the components of $\underline{n}(t)$ by \mathcal{N} , we further define the (discrete for now) density field configuration $\underline{\phi}(t) \equiv (\vec{\phi}_1(t), \vec{\phi}_2(t), \dots, \vec{\phi}_M(t))$ where $\vec{\phi}_i(t) = (\phi_i^X(t), \phi_i^Y(t))$ with $\phi_i^m(t) = n_i^m(t)/\mathcal{N}$.

1. The utility function

An agent of type a at lattice site i has a measure of the *utility* of the configuration in which it finds itself, $\pi_i^a(\underline{\phi}(t))$. The utility π_i^a generically depends on the configuration and on the lattice site i .

While we do not consider utility functions that explicitly depend on the latter in this work, we note that adding this feature may be necessary for a more realistic description of human residential dynamics.

As noted by Schelling himself [69], any model for residential dynamics that is built only on neighborhood composition preferences ignores at least 2 other factors largely responsible for observed residential patterns – discrimination (e.g. redlining) and socioeconomic inequality (e.g. income inequality). In either case, the end result is that certain areas in space are more or less accessible to certain groups as imposed by factors other than their own personal preference. These effects can be at least partially captured by adding an explicit, spatially dependent term to the utility functions which acts like an externally imposed potential function restricting movement. For example, one could consider $\pi_i^a(\underline{\phi}) = \alpha i + f(\underline{\phi})$, where α is a constant that determines the utility of a location i , in addition to a term $f(\underline{\phi})$ that captures the individuals preferences. For the rest of this work, however, we only consider utilities that are functions of the system configuration, $\pi^a(\vec{\phi}_i) = \pi^a(\phi_i^X, \phi_i^Y)$. Finally, we note that each individual does not count itself as a neighbor in the evaluation of its utility, e.g. an individual of type X calculates its utility as $\pi^X(\vec{\phi}_i) = \pi^X(\phi_i^X - \mathcal{N}^{-1}, \phi_i^Y)$.

2. The transition rates

An individual of type b moves by jumping from site j to site k . This changes the configuration as

$$\underline{\phi} \rightarrow \underline{\phi}' = D_{k|j}^b \underline{\phi} \quad \text{such that} \quad (D_{k|j}^b \underline{\phi})_i^a = \phi_i^a + \delta^{ab} (\delta_{ik} - \delta_{ij}) \delta \phi, \quad (19)$$

where $\delta \phi = \mathcal{N}^{-1}$. We have defined the *diffusion operator* $D_{k|j}^b$ that acts on the configuration $\underline{\phi}$ by removing an individual of type b from site j and adding it to site k .

An individual makes this jump with a probability depending on a gain function, $g^a(k|j)$, which measures the variation of its utility after moving from site j to site k .

The rate we consider is similar to those used in Glauber dynamics of spin lattices [188], as well as in other quantitative socioeconomic models where it is known as a logit function [9, 121],

$$w^a(k|j) = w^a(g^a(k|j)) = \frac{\tau^{-1}}{1 + \exp(-g^a(k|j)/T)}, \quad (20)$$

where τ gives a time scale for the jumps and T is akin to a temperature that quantifies the uncertainty of a move decreasing the gain function.

We note that Eq. 20 is not the only choice possible. Generically, the transition rate should satisfy certain properties, namely $w^a(g \rightarrow \infty) \rightarrow 1$ and $w^a(g \rightarrow -\infty) = 0$. The logit transition rate, in addition of satisfying these properties, also obeys detailed balance when $g^a(k|j) = G(k) - G(j)$, *i.e.* when the gain can be written as the difference of some function G that only depends on the system configuration. If the latter is verified, detailed balance holds and the

system will settle into a steady state given by the Boltzmann Distribution of statistical physics, $p(\underline{\phi}) \propto e^{G/T}$. This was pointed out for socioeconomic agents in [9].

In this work, we take the gain to be given by

$$g^a(k|j) = g^a(\vec{\phi}_k, \vec{\phi}_j) = (1 - \alpha) \left[\pi^a(\vec{\phi}_k) - \pi^a(\vec{\phi}_j) \right] + \alpha \left[U[\underline{\phi}'] - U[\underline{\phi}] \right] + \Gamma \left[\Sigma[\underline{\phi}'] - \Sigma[\underline{\phi}] \right]. \quad (21)$$

The first term in Eq. (21) denotes the change in the moving particle's own utility before and after the move. The second term denotes the change in the global utility given by the functional $U[\underline{\phi}]$,

$$U[\underline{\phi}] = \mathcal{N} \sum_{b=X,Y} \sum_{j=1}^M \phi_j^b \pi^b(\vec{\phi}_j). \quad (22)$$

From here, we see that the parameter $\alpha \in [0, 1]$ denotes the relative weight that a particle gives to its own utility with respect to the utility of the entire system. For this reason, we follow [9] and call α an *altruism parameter*. Completely selfish particles ($\alpha = 0$) only consider their own utility, while completely altruistic particles ($\alpha = 1$) only consider the utility of the global configuration. We note that the main text only considered $\alpha = 0$.

The functional $\Sigma[\underline{\phi}]$ denotes a contribution to the gain that comes from spatial gradients of the density field,

$$\Sigma[\underline{\phi}] = \mathcal{N} \sum_{b=X,Y} \sum_{j=1}^M \phi_j^b \left(\partial_x^2 \phi \right)_j^b. \quad (23)$$

Here, $\partial_x^2 \phi$ is a discrete Laplacian operator defined as

$$\left(\partial_x^2 \phi \right)_j^b = \frac{\phi_{j+1}^b - 2\phi_j^b + \phi_{j-1}^b}{\ell^2}. \quad (24)$$

This function indicates that particles like being at a minimum of the density field, where $\partial_x^2 \phi > 0$. We will see that this term gives the system a surface tension that promotes spatial uniformity in the density field. Intuitively, this comes from the fact that particles are more likely to move into local minima of the density field ($\partial_x^2 \phi > 0$) and away from local maxima of the density field ($\partial_x^2 \phi < 0$), thereby reducing local gradients in the density field. This will prove crucial to obtain a well-behaved hydrodynamic theory.

F. Derivation of sociohydrodynamic equations

Here we detail our derivation of the sociohydrodynamic equations in the main text.

The stochastic evolution of the system is described by the probability distribution $P(\underline{n}, t)$, which is assumed to obey the master equation

$$\partial_t P(\underline{n}, t) = \sum_{\underline{n}'} W(\underline{n}|\underline{n}') P(\underline{n}', t) - W(\underline{n}'|\underline{n}) P(\underline{n}, t), \quad (25)$$

where $W(\underline{n}'|\underline{n})$ is the transition rate from state \underline{n} to state \underline{n}' and $\sum_{\underline{n}'}$ is a sum over all system configurations.

The allowed transitions are given by Eq. (19), which reduce the sum over configurations to sums over particle types and pairs of sites jk

$$\partial_t P(\underline{n}, t) = \sum_{b=X,Y} \sum_{jk} W(\underline{n}|D_{k|j}^b \underline{n}) P(D_{k|j}^b \underline{n}, t) - W(D_{k|j}^b \underline{n}|\underline{n}) P(\underline{n}, t). \quad (26)$$

We can now find the dynamics for the average number of particles of type a at lattice site i ,

$$\partial_t \langle n_i^a \rangle(t) = \sum_{\underline{n}} n_i^a \partial_t P(\underline{n}, t) \quad (27a)$$

$$= \sum_{\underline{n}} n_i^a \left(\sum_b \sum_{jk} W(\underline{n}|D_{k|j}^b \underline{n}) P(D_{k|j}^b \underline{n}, t) - W(D_{k|j}^b \underline{n}|\underline{n}) P(\underline{n}, t) \right) \quad (27b)$$

$$= \sum_{\underline{n}} \sum_b \sum_{jk} n_i^a W(\underline{n}|D_{k|j}^b \underline{n}) P(D_{k|j}^b \underline{n}, t) - n_i^a W(D_{k|j}^b \underline{n}|\underline{n}) P(\underline{n}, t). \quad (27c)$$

We wish to make the right hand side the average over some function of n_i^a , i.e. $\partial_t \langle n_i^a \rangle = \langle f(n_i^a) \rangle = \sum_{\underline{n}} P(\underline{n}, t) f(n_i^a)$ in order to apply the mean-field approximation, i.e. $\partial_t \langle n_i \rangle = f(\langle n_i \rangle)$. To this end, we perform a change of variables in the first term of Eq. (27c), taking

$$\underline{n} \rightarrow D_{j|k}^b \underline{n} = \left(D_{k|j}^b \right)^{-1} \underline{n}$$

This change of variables leaves the sum over configurations unchanged as both $D_{k|j}^b$ and $D_{j|k}^b$ preserve particle number. This gives

$$\partial_t \langle n_i \rangle(t) = \sum_{\underline{n}} \sum_b \sum_{jk} (D_{j|k}^b \underline{n})_i^a W(D_{j|k}^b \underline{n} | \underline{n}) P(\underline{n}, t) - n_i^a W(D_{k|j}^b \underline{n} | \underline{n}) P(\underline{n}, t) \quad (28a)$$

$$= \sum_{\underline{n}} P(\underline{n}, t) \sum_b \sum_{jk} (D_{j|k}^b \underline{n})_i^a W(D_{j|k}^b \underline{n} | \underline{n}) - n_i^a W(D_{k|j}^b \underline{n} | \underline{n}) \quad (28b)$$

$$= \left\langle \sum_b \sum_{jk} (D_{j|k}^b \underline{n})_i^a W(D_{j|k}^b \underline{n} | \underline{n}) - n_i^a W(D_{k|j}^b \underline{n} | \underline{n}) \right\rangle. \quad (28c)$$

In the following, we take the mean-field approximation and drop the angle brackets.

As written, $W(D_{k|j}^b \underline{n} | \underline{n})$ gives the rate for *some* particle of type b to move from site j to site k in the configuration \underline{n} . This is not the single particle jump rate given by Eq. 20, $w^b(k|j)$. Rather, the two are related by

$$W(D_{k|j}^b \underline{n} | \underline{n}) = n_j^b \left(1 - \sum_c \phi_k^c \right) w^b(k|j) (\delta_{k,j+1} + \delta_{k,j-1}). \quad (29)$$

Intuitively, the above formula states that the rate at which a b particle moves from site j to site k is given by the rate at which a single b particle makes that transition ($w^b(k|j)$) scaled by the number of b particles at j (n_j^b) and the fraction of vacant sites at k ($1 - \sum_c \phi_k^c$). This prevents particles from entering full sites. In the following, we denote the total vacancy fraction by

$$\psi_k = 1 - \sum_c \phi_k^c.$$

Finally, we have also restricted motion to neighboring lattice sites, specifying that $k = j \pm 1$ with the Kronecker deltas.

Plugging this decomposition of $W(D_{k|j}^b \underline{n} | \underline{n})$ into the mean-field equation (28c) and writing $(D_{j|k}^b \underline{n})_i^a$ explicitly, we obtain

$$\begin{aligned} \partial_t n_i^a = & \sum_b \sum_{jk} \left(n_i^a + \delta^{ab} (\delta_{ij} - \delta_{ik}) \right) n_k^b \psi_j w^b(j|k) (\delta_{j,k+1} + \delta_{j,k-1}) \\ & - n_i^a n_j^b \psi_k w^b(k|j) (\delta_{k,j+1} + \delta_{k,j-1}). \end{aligned} \quad (30)$$

The first and last terms cancel as they are identical up to a relabeling of $j \leftrightarrow k$ and are summed over all j, k . After summing over b in the middle term, we have

$$\partial_t n_i^a = \sum_{jk} n_k^a \psi_j w^a(j|k) (\delta_{ij} - \delta_{ik}) (\delta_{j,k+1} + \delta_{j,k-1}). \quad (31)$$

The sum over jk is significantly simplified due to the two sets of δ -functions and gives

$$\partial_t n_i^a = n_{i-1}^a \psi_i w^a(i|i-1) + n_{i+1}^a \psi_i w^a(i|i+1) - n_i^a [\psi_{i-1} w^a(i-1|i) + \psi_{i+1} w^a(i+1|i)]. \quad (32)$$

This has the form of a conservation law,

$$\begin{aligned} \partial_t n_i^a = & J_{i-1}^a - J_i^a \\ J_i^a = & n_i^a \psi_{i+1} w^a(i+1|i) - n_{i+1}^a \psi_i w^a(i+1|i) \end{aligned} \quad (33)$$

Moving to continuous space, the lattice site i is at position $x = il$, where ℓ is the lattice spacing. Upon taking $l \rightarrow 0$ and dividing by \mathcal{N} , we can approximate the above as

$$\partial_t \phi^a(x, t) = j^a(x-l) - j^a(x) \approx -l \partial_x j^a(x) \quad (34)$$

Now we are left to specify the particle current,

$$j^a(x) = \phi^a(x)\psi(x+\ell)w^a(x+\ell|x) - \phi^a(x+\ell)\psi(x)w^a(x|x+\ell) \quad (35)$$

Performing a Taylor expansion for $\ell \rightarrow 0$ up to $\mathcal{O}(\ell^2)$ gives

$$\begin{aligned} j^a(x) &= \phi^a(\psi + \ell\partial_x\psi) \left(w^a(x|x) + \ell\partial_x\vec{\phi} \cdot \nabla_{\vec{\phi}}^{(1|0)} w^a(x|x) \right) - (\phi^a + \ell\partial_x\phi^a)\psi \left(w^a(x|x) + \ell\partial_x\vec{\phi} \cdot \nabla_{\vec{\phi}}^{(0|1)} w^a(x|x) \right) + \mathcal{O}(\ell^2) \\ j^a(x) &= \ell \left[(\phi^a\partial_x\psi - \psi\partial_x\phi^a) w^a(x|x) + \phi^a\psi\partial_x\vec{\phi} \cdot \left(\nabla_{\vec{\phi}}^{(1|0)} w^a(x|x) - \nabla_{\vec{\phi}}^{(0|1)} w^a(x|x) \right) \right] + \mathcal{O}(\ell^2), \end{aligned} \quad (36)$$

where we have canceled all terms $\mathcal{O}(\ell^0)$. Furthermore, we have used the notation $\partial_x\vec{\phi} = (\partial_x\phi^X, \partial_x\phi^Y)$,

$$\nabla_{\vec{\phi}}^{(\mu|\nu)} w^a(y|x) = \begin{pmatrix} \partial_{\phi^X}^{(\mu|\nu)} w^a(y|x) \\ \partial_{\phi^Y}^{(\mu|\nu)} w^a(y|x) \end{pmatrix} \quad (37)$$

and

$$\partial_{\phi^b}^{(\mu|\nu)} w^a(y|x) = \frac{\partial^{\mu+\nu} w^a(y|x)}{\partial \phi^b(y)^\mu \partial \phi^b(x)^\nu}. \quad (38)$$

Finally, we take $f(x|x) = \lim_{y,z \rightarrow x} f(y|z)$ for any function $f(y|z)$.

We are left to evaluate $w^a(x|x)$ and its derivatives. We begin with the former, which amounts to calculating $g^a(x|x)$. Recalling Eq. 21, we rewrite it in continuous space variables as

$$g^a(y|x) = (1-\alpha) \left(\pi^a(\vec{\phi}(y) + \delta\phi\hat{e}_a) - \pi^a(\vec{\phi}(x)) \right) + \alpha \left(U[D^a(y|x)\vec{\phi}(x')] - U[\vec{\phi}(x')] \right) + \Gamma \left(\Sigma[D^a(y|x)\vec{\phi}(x')] - \Sigma[\vec{\phi}(x')] \right), \quad (39)$$

where we have introduced the notation \hat{e}_a which is a vector with one in the a component, and zero otherwise. This is simply a convenient way to specify that the fraction only changes in the a species when considering g^a . Furthermore, there is a dummy index x' in the arguments of U and Σ , reflecting the fact that these functionals will be integrated over x' .

The continuous version of the diffusion operator takes the form

$$D^a(y|x)\vec{\phi}(x') = \phi^b(x') + \delta\phi\delta^{ab} (\delta(x'-y) - \delta(x'-x))$$

The second term of the gain is given by

$$\begin{aligned} U[D^a(y|x)\vec{\phi}(x')] - U[\vec{\phi}(x')] &= \mathcal{N} \sum_{b=X,Y} \int dx' \left[\left(D^a(y|x)\vec{\phi}(x') \right) \pi^b \left(D^a(y|x)\vec{\phi}(x') \right) - \phi^b(x') \pi^b(\vec{\phi}(x')) \right] \\ &= \mathcal{N} \sum_b \left(\phi^b(y) + \delta\phi\delta^{ab} \right) \pi^b \left(\vec{\phi}(y) + \delta\phi\hat{e}^a \right) - \phi^b(y) \pi^b(\vec{\phi}(y)) \\ &\quad + \left(\phi^b(x) - \delta\phi\delta^{ab} \right) \pi^b \left(\vec{\phi}(x) - \delta\phi\hat{e}^a \right) - \phi^b(x) \pi^b(\vec{\phi}(x)). \end{aligned} \quad (40)$$

A similar calculation can be done for the third term proportional to Γ . With great care taken to keep track of all the correct indices, we only report the result,

$$\Sigma[D^a(y|x)\vec{\phi}(x')] - \Sigma[\vec{\phi}(x)] = \partial_x^2 \phi^a(y) - \partial_x^2 \phi^a(x) - 3\delta\phi. \quad (41)$$

Combining the above equations, we arrive at

$$g^a(x|x) \approx \delta\phi \left[(1-\alpha) \frac{\partial \pi^a}{\partial \phi^a} + \alpha \frac{\partial^2 u}{(\partial \phi^a)^2} - 3 \right] \quad (42)$$

where the Laplacian terms in Σ cancelled when $y=x$. In the limit where $\delta\phi \rightarrow 0$, this term goes to zero, making

$$\lim_{\delta\phi \rightarrow 0} w^a(x|x) = w^a(g^a=0) = \frac{\tau^{-1}}{2}. \quad (43)$$

We now turn to computing the derivatives of the rate functions,

$$\partial_{\phi^b}^{(1|0)} w^a(y|x) = \frac{\partial w^a(y|x)}{\partial \phi^b(y)} = \frac{dw^a(g^a)}{dg^a} \frac{\partial g^a(\vec{\phi}(y), \vec{\phi}(x))}{\partial \phi^b(y)}. \quad (44)$$

The first factor in the above equation is given by

$$\frac{dw^a}{dg^a} = \frac{\tau^{-1}}{(1 + e^{-g^a/T})^2} \frac{e^{-g^a/T}}{T}, \quad (45)$$

and in the limit of vanishing $\delta\phi$ it reduces to

$$\frac{dw^a}{dg^a} \xrightarrow{\delta\phi \rightarrow 0} \frac{\tau^{-1}}{4T}. \quad (46)$$

To close (44), we need to compute the derivatives of the gain g^a with respect to the fields using expression (39). Substituting the final form of (44) into (36) will then give the expression of the hydrodynamic current. We first consider the case $\Gamma = 0$ and will discuss how to include the Γ -dependent contributions to the current later. Retaining only the terms proportional to α and $(1 - \alpha)$ in Eq. 39, we derive them with respect to $\phi^b(y)$ before taking the limit $\delta\phi \rightarrow 0$ to obtain

$$\left. \frac{\partial g^a(y|x)}{\partial \phi^b(y)} \right|_{y=x} \xrightarrow{\delta\phi \rightarrow 0} (1 - \alpha) \frac{\partial \pi^a}{\partial \phi^b} + \alpha \frac{\partial^2 u}{\partial \phi^a \partial \phi^b}, \quad (47)$$

where $u(x, t) = \phi^X \pi^X(\vec{\phi}(x)) + \phi^Y \pi^Y(\vec{\phi}(x))$. Performing a similar computation, we also obtain

$$\lim_{\delta\phi \rightarrow 0} \left. \frac{\partial g^a(y|x)}{\partial \phi^b(x)} \right|_{y=x} = - \lim_{\delta\phi \rightarrow 0} \left. \frac{\partial g^a(y|x)}{\partial \phi^b(y)} \right|_{y=x}. \quad (48)$$

Inserting (47) into (44), we obtain the derivative of the jump rate as

$$-\partial_{\phi^b}^{(0|1)} w^a(x|x) = \partial_{\phi^b}^{(1|0)} w^a(x|x) = \frac{\tau^{-1}}{4T} \left((1 - \alpha) \frac{\partial \pi^a}{\partial \phi^b} + \alpha \frac{\partial^2 u}{\partial \phi^a \partial \phi^b} \right). \quad (49)$$

We can now inject (49) and (43) in expression (36) to obtain the particle current j_0^a in the $\Gamma = 0$ case as

$$j_0^a(x) = \frac{\ell\tau^{-1}}{2} \left[(\phi^a \partial_x \psi - \psi \partial_x \phi^a) - T^{-1} \phi^a \psi \left((1 - \alpha) \partial_x \pi^a + \alpha \partial_x \frac{\partial u}{\partial \phi^a} \right) \right]. \quad (50)$$

When $\Gamma \neq 0$, additional contributions have to be taken into account in (50). We now discuss what are these contributions due to a nonzero Γ . Instead of deriving them by using expression (44) together with (39), which is not a straightforward derivation due to the presence of both functional and spatial gradients, we will use arguments drawn from equilibrium physics. First, we note that the term proportional to Γ in (39) is a purely relaxational, equilibrium contribution to the gain. Indeed, it is written as a difference of a single function evaluated before and after the microscopic jump. Having a gain function with this property necessarily gives rise to a Boltzmann-like steady-state distribution with a well-defined potential function $F[\vec{\phi}(x)]$. In the case of the Σ functional, which penalizes gradients, this potential function is given by $F[\vec{\phi}(x)] = |\partial_x \phi^a|^2/2$. Taking into account volume exclusions, the contribution j_Γ^a to the current due to the gradient-penalizing terms is given by the equilibrium formula $j_\Gamma^a = M^{ab}(\vec{\phi}) \partial_x \delta F / \delta \phi^b$, with a fraction-dependent mobility $M^{ab}(\vec{\phi}) = \delta^{ab} \phi^b \psi$. Inserting the expression $F[\vec{\phi}(x)] = |\partial_x \phi^a|^2/2$ in the latter formula for j_Γ^a gives

$$j_\Gamma^a = \Gamma^a \phi^a \psi \partial_x^3 \phi^a. \quad (51)$$

Adding the above contribution to (50) gives us the final form of the current as

$$j^a(x) = j_0^a(x) + j_\Gamma^a(x) = \frac{\ell\tau^{-1}}{2} \left[(\phi^a \partial_x \psi - \psi \partial_x \phi^a) - T^{-1} \phi^a \psi \left((1 - \alpha) \partial_x \pi^a + \alpha \partial_x \frac{\partial u}{\partial \phi^a} + \Gamma^a \partial_x^3 \phi^a \right) \right]. \quad (52)$$

We now make an assumption about the rate of jumping τ : we assume that it follows an Eyring equation [189] with $\tau \propto T$. The latter indicates that reactions happen faster as the temperature increases. In particular, we assume $\tau = 2T$. In this case, the current becomes

$$j^a(x) = \ell \left[T (\phi^a \partial_x \psi - \psi \partial_x \phi^a) - \phi^a \psi \left((1 - \alpha) \partial_x \pi^a + \alpha \frac{\partial u}{\partial \phi^a} + \Gamma^a \partial_x^3 \phi^a \right) \right]. \quad (53)$$

Using (53) into (34) and setting the unit length such that $l = 1$, we arrive at our sociohydrodynamics equation

$$\begin{aligned} \partial_t \phi^a(x, t) &= T \left((1 - \phi^b) \partial_x^2 \phi^a + \phi^a \partial_x^2 \phi^b \right) - \partial_x \left(\phi^a \psi \left[(1 - \alpha) \partial_x \pi^a + \alpha \partial_x \frac{\partial u}{\partial \phi^a} + \Gamma \partial_x^3 \phi^a \right] \right) \\ &= -\partial_x \left(\sum_b D^{ab}(\vec{\phi}) \partial_x \phi^b + \Gamma \mu^a(\vec{\phi}) \partial_x^3 \phi^a \right) \end{aligned} \quad (54)$$

where D^{ab} are the elements of the matrix

$$\mathbb{D}(\vec{\phi}) = -T \begin{pmatrix} 1 - \phi^Y & \phi^X \\ \phi^Y & 1 - \phi^X \end{pmatrix} + \psi \begin{pmatrix} \phi^X \left((1 - \alpha) \frac{\partial \pi^X}{\partial \phi^X} + \alpha \frac{\partial^2 u}{(\partial \phi^X)^2} \right) & \phi^X \left((1 - \alpha) \frac{\partial \pi^X}{\partial \phi^Y} + \alpha \frac{\partial^2 u}{\partial \phi^X \partial \phi^Y} \right) \\ \phi^Y \left((1 - \alpha) \frac{\partial \pi^Y}{\partial \phi^X} + \alpha \frac{\partial^2 u}{\partial \phi^X \partial \phi^Y} \right) & \phi^Y \left((1 - \alpha) \frac{\partial \pi^Y}{\partial \phi^Y} + \alpha \frac{\partial^2 u}{(\partial \phi^Y)^2} \right) \end{pmatrix}. \quad (55)$$

Generically, the diffusion matrix can be written as

$$\mathbb{D}(\vec{\phi}) = \begin{pmatrix} D^{XX} & D_+ - D_- \\ D_+ + D_- & D^{YY} \end{pmatrix}. \quad (56)$$

Taking the equal density regime, $\vec{\phi} = (\phi, \phi)$, the off-diagonal terms are given by

$$D_+ = \frac{D^{XY} + D^{YX}}{2} = -T\phi + \frac{\phi(1 - 2\phi)}{2} \left[(1 - \alpha) \left(\frac{\partial \pi^X}{\partial \phi^Y} + \frac{\partial \pi^Y}{\partial \phi^X} \right) + 2\alpha \frac{\partial^2 u}{\partial \phi^X \partial \phi^Y} \right] \quad (57a)$$

$$D_- = \frac{D^{YX} - D^{XY}}{2} = \frac{\phi(1 - 2\phi)}{2} (1 - \alpha) \left(\frac{\partial \pi^Y}{\partial \phi^X} - \frac{\partial \pi^X}{\partial \phi^Y} \right). \quad (57b)$$

From (57b), we see that, when the densities of both species are equal, the antisymmetric part of $\mathbb{D}(\vec{\phi})$ $\vec{\phi} = (\phi, \phi)$ directly measures the breaking of the compatibility condition.

G. The potential function

The advantage of using Eq. (20) as the transition rate is its connection to detailed balance. Namely, if one can show that

$$g^a(k|j) = F[\underline{\phi}'] - F[\underline{\phi}],$$

then the system obeys detailed balance and will settle into a steady state given by the Boltzmann distribution, $P(\underline{\phi}) \propto e^{F[\underline{\phi}]/T}$ [190]. To find this potential function, $F[\underline{\phi}]$, we will proceed term by term in Eq. (21) and show that they can each be written as the difference of some function depending on $\underline{\phi}$. The full potential function will then be a sum of these individual contributions.

This condition is manifestly satisfied by the second and third terms in Eq. (21), which are already written in the requisited form of a difference of a function of $\underline{\phi}$. However, it is not immediately obvious that the first term can be written as a function of the full configuration, as it explicitly depends on the type of particle moving (i.e. has a dependence on the index a) and on the specific lattice sites in consideration (i.e. has dependence on the indices j, k).

Luckily, [9] showed that it is indeed possible if the utilities obey a specific restriction. Specifically, the function is given by

$$L(\underline{\phi}) = \frac{1}{2} \sum_i \left[\sum_{n=0}^{n_i^X-1} \left(\pi^X \left(\frac{n}{\mathcal{N}}, \frac{n_i^Y-1}{\mathcal{N}} \right) + \pi^X \left(\frac{n}{\mathcal{N}}, 0 \right) \right) + \sum_{m=0}^{n_i^Y-1} \left(\pi^Y \left(\frac{n_i^X}{\mathcal{N}}, \frac{m}{\mathcal{N}} \right) + \pi^Y \left(0, \frac{m}{\mathcal{N}} \right) \right) \right], \quad (58)$$

and the restriction on the utilities is

$$\pi^X \left(\frac{n^X}{\mathcal{N}}, \frac{n^Y+1}{\mathcal{N}} \right) - \pi^X \left(\frac{n^X}{\mathcal{N}}, \frac{n^Y}{\mathcal{N}} \right) = \pi^Y \left(\frac{n^X+1}{\mathcal{N}}, \frac{n^Y}{\mathcal{N}} \right) - \pi^Y \left(\frac{n^X}{\mathcal{N}}, \frac{n^Y}{\mathcal{N}} \right). \quad (59)$$

This is the discrete version of the compatibility condition introduced in the main text. In the next section, we explicitly show that $L(\underline{\phi})$ is indeed a potential function for the first term of Eq. (21).

We are now in a position to give the form of our potential function, $F[\underline{\phi}]$, where we follow § 4.1.1 in [187]. As stated above, given the satisfaction of Eq. (59), our system will reach a steady state given by

$$P[\underline{\phi}] = \frac{1}{Z} \exp \left(\frac{\mathcal{N}}{T} \tilde{F}[\underline{\phi}] \right)$$

where Z is a normalization factor. The potential function can be written as a sum over lattice sites,

$$\tilde{F}[\underline{\phi}] = \sum_i \tilde{f}(\vec{\phi}_i),$$

with the density

$$\tilde{f}(\vec{\phi}_i) = T \tilde{S}(\vec{\phi}_i) + (1 - \alpha) \tilde{\ell}(\vec{\phi}_i) + \alpha \tilde{u}(\vec{\phi}_i) + \Gamma \tilde{\sigma}(\vec{\phi}_i) \quad (60a)$$

$$\tilde{S}(\vec{\phi}_i) = \frac{1}{\mathcal{N}} \ln \left(\frac{\mathcal{N}!}{n_i^X! n_i^Y! (\mathcal{N} - n_i^X - n_i^Y)!} \right) \quad (60b)$$

$$\tilde{\ell}(\vec{\phi}_i) = \frac{1}{2\mathcal{N}} \left[\sum_{n=0}^{n_i^X-1} \pi^X \left(\frac{n}{\mathcal{N}}, \frac{n_i^Y-1}{\mathcal{N}} \right) + \pi^X \left(\frac{n}{\mathcal{N}}, 0 \right) + \sum_{m=0}^{n_i^Y-1} \pi^Y \left(\frac{n_i^X}{\mathcal{N}}, \frac{m}{\mathcal{N}} \right) + \pi^Y \left(0, \frac{m}{\mathcal{N}} \right) \right] \quad (60c)$$

$$\tilde{u}(\vec{\phi}_i) = \sum_{b=X,Y} \phi^b \pi^b(\vec{\phi}_i) \quad (60d)$$

$$\tilde{\sigma}(\vec{\phi}_i) = \sum_{b=X,Y} \frac{\phi_i^b (\partial_x^2 \phi_i^b)}{2}. \quad (60e)$$

The term $S(\vec{\phi}_i)$ comes from counting the number of ways of arranging n^X and n^Y particles in a lattice site with \mathcal{N} total sites. Taking the limit $\{\mathcal{N}, n_i^a\} \rightarrow \infty$ while keeping $\phi_i^a = n_i^a/\mathcal{N}$ constant, we can expand the factorials in \tilde{S} using Stirling's approximation, $\ln n! \approx n \ln n - n$, to get

$$\tilde{S}(\vec{\phi}_i) \rightarrow S(\vec{\phi}_i) = -\phi_i^X \ln \phi_i^X - \phi_i^Y \ln \phi_i^Y - \psi_i \ln \psi_i, \quad (61)$$

where $\psi_i = 1 - \phi_i^X - \phi_i^Y$ is the number of vacancies at site i . This is the entropy of mixing.

Furthermore, we can convert the sums in $\tilde{\ell}(\vec{\phi}_i)$ to integrals, giving

$$\tilde{\ell}(\vec{\phi}_i) \rightarrow \ell(\vec{\phi}_i) = \frac{1}{2} \left[\int_0^{\phi_i^X} d\psi \pi^X(\psi, \phi_i^Y) + \pi^X(\psi, 0) + \int_0^{\phi_i^Y} d\psi' \pi^Y(\phi_i^X, \psi') + \pi^Y(0, \psi') \right]. \quad (62)$$

Finally, we also take the continuum limit, $l \rightarrow 0$, while keeping the total density, $\sum_i \phi_i^a \rightarrow l^{-1} \int \phi^a(x) dx$ constant. For all the local terms, this amounts to converting discrete i indices to a continuous x coordinate. In addition, the discrete Laplacian operator in $\sigma(\vec{\phi}_i)$ becomes the usual differential Laplacian operator.

We now finally arrive at our potential function,

$$F[\vec{\phi}(x)] = \int f(\vec{\phi}(x)) dx$$

with the potential density

$$f(\vec{\phi}, \partial_x \vec{\phi}) = TS(\vec{\phi}) + (1 - \alpha)\ell(\vec{\phi}) + \alpha u(\vec{\phi}) - \Gamma\sigma(\vec{\phi}) \quad (63a)$$

$$S(\vec{\phi}) = -\phi^X \ln(\phi^X) - \phi^Y \ln(\phi^Y) - \psi \ln \psi \quad (63b)$$

$$\ell(\vec{\phi}) = \frac{1}{2} \left[\int_0^{\phi^X} d\psi \left(\pi^X(\psi, \phi^Y) + \pi^X(\psi, 0) \right) + \int_0^{\phi^Y} d\psi' \left(\pi^Y(\phi^X, \psi') + \pi^Y(0, \psi') \right) \right] \quad (63c)$$

$$u(\vec{\phi}) = \sum_{a=X,Y} \phi^a \pi^a(\vec{\phi}) \quad (63d)$$

$$\sigma(\vec{\phi}) = \sum_{a=X,Y} \frac{|\partial_x \phi^a(x)|^2}{2} \quad (63e)$$

Note that we have used integration by parts on $\int \sigma(\vec{\phi}(x)) dx$ to obtain the minus sign in front of Γ . In the large \mathcal{N} limit, the compatibility condition Eq. 59 is now given by

$$\frac{\partial \pi^X}{\partial \phi^Y} = \frac{\partial \pi^Y}{\partial \phi^X} \quad (64)$$

1. Demonstration of $L(\underline{\phi})$ as a potential function

Here, we will explicitly show

$$L(\underline{\phi}') - L(\underline{\phi}) = \pi^a(\vec{\phi}'_k) - \pi^a(\vec{\phi}'_j) = \pi^a(\vec{\phi}'_k) - \pi^a(\vec{\phi}'_j - \delta\phi \hat{e}_a),$$

where $\underline{\phi}' = D_{k|j}^a \underline{\phi}$. For concreteness, let us set $a = X$. The calculation for $a = Y$ proceeds identically. In this case,

$$L(D_{k|j}^X \underline{\phi}) = \frac{1}{2} \sum_i \left[\sum_{n'=0}^{n_i^X - 1 + \delta_{ik} + \delta_{ij}} \pi^X \left(\frac{n'}{\mathcal{N}}, \frac{n_i^Y}{\mathcal{N}} \right) + \pi^X \left(\frac{n'}{\mathcal{N}}, 0 \right) + \sum_{m'=0}^{n_i^Y - 1} \pi^Y \left(\frac{n_i^X - 1 + \delta_{ik} - \delta_{ij}}{\mathcal{N}}, \frac{m'}{\mathcal{N}} \right) + \pi^Y \left(0, \frac{m'}{\mathcal{N}} \right) \right]. \quad (65)$$

Each term in the sum over i in $L(\underline{\phi}') - L(\underline{\phi})$ is zero unless $i = \{j, k\}$. We are left with

$$\begin{aligned} 2(L(D_{k|j}^X \underline{\phi}) - L(\underline{\phi})) &= \sum_{n'_k=0}^{n_k^X} \pi^X \left(\frac{n'_k}{\mathcal{N}}, \frac{n_k^Y}{\mathcal{N}} \right) + \pi^X \left(\frac{n'_k}{\mathcal{N}}, 0 \right) + \sum_{m'_k=0}^{n_k^Y - 1} \pi^Y \left(\frac{n_k^X + 1}{\mathcal{N}}, \frac{m'_k}{\mathcal{N}} \right) + \pi^Y \left(0, \frac{m'_k}{\mathcal{N}} \right) \\ &\quad - \sum_{n_k=0}^{n_k^X - 1} \pi^X \left(\frac{n_k}{\mathcal{N}}, \frac{n_k^Y}{\mathcal{N}} \right) + \pi^X \left(\frac{n_k}{\mathcal{N}}, 0 \right) - \sum_{m_k=0}^{n_k^Y - 1} \pi^Y \left(\frac{n_k^X}{\mathcal{N}}, \frac{m_k}{\mathcal{N}} \right) + \pi^Y \left(0, \frac{m_k}{\mathcal{N}} \right) \\ &\quad + \sum_{n'_j=0}^{n_j^X - 2} \pi^X \left(\frac{n'_j}{\mathcal{N}}, \frac{n_j^Y}{\mathcal{N}} \right) + \pi^X \left(\frac{n'_j}{\mathcal{N}}, 0 \right) + \sum_{m'_j=0}^{n_j^Y - 1} \pi^Y \left(\frac{n_j^X - 1}{\mathcal{N}}, \frac{m'_j}{\mathcal{N}} \right) + \pi^Y \left(0, \frac{m'_j}{\mathcal{N}} \right) \\ &\quad - \sum_{n_j=0}^{n_j^X - 1} \pi^X \left(\frac{n_j}{\mathcal{N}}, \frac{n_j^Y}{\mathcal{N}} \right) + \pi^X \left(\frac{n_j}{\mathcal{N}}, 0 \right) - \sum_{m_j=0}^{n_j^Y - 1} \pi^Y \left(\frac{n_j^X}{\mathcal{N}}, \frac{m_j}{\mathcal{N}} \right) + \pi^Y \left(0, \frac{m_j}{\mathcal{N}} \right). \end{aligned} \quad (66)$$

The first two lines come from the $i = k$ term of $L(\underline{\phi}') - L(\underline{\phi})$, while the final two lines from the $i = j$ term of $L(\underline{\phi}') - L(\underline{\phi})$, respectively. We have color-coded the different terms for clarity in what follows.

To proceed, we notice that the very last terms in the first two lines cancel, as do the very last terms in the final two lines. Combining the remaining terms with the same colors, we have

$$\begin{aligned}
2(L(D_{k|j}^X \underline{\phi}) - L(\underline{\phi})) &= \pi^X \left(\frac{n_k^X}{\mathcal{N}}, \frac{n_k^Y}{\mathcal{N}} \right) + \pi^X \left(\frac{n_k^X}{\mathcal{N}}, 0 \right) - \pi^X \left(\frac{n_j^X - 1}{\mathcal{N}}, \frac{n_j^Y}{\mathcal{N}} \right) - \pi^X \left(\frac{n_j^X - 1}{\mathcal{N}}, 0 \right) \\
&+ \sum_{m_k=0}^{n_k^Y-1} \pi^Y \left(\frac{n_k^X + 1}{\mathcal{N}}, \frac{m_k}{\mathcal{N}} \right) - \pi^Y \left(\frac{n_k^X}{\mathcal{N}}, \frac{m_k}{\mathcal{N}} \right) + \sum_{m_j=0}^{n_j^Y-1} \pi^Y \left(\frac{n_j^X - 1}{\mathcal{N}}, \frac{m_j}{\mathcal{N}} \right) - \pi^Y \left(\frac{n_j^X}{\mathcal{N}}, \frac{m_j}{\mathcal{N}} \right).
\end{aligned} \tag{67}$$

Here, we are forced to use Eq. (59) to change the last two summands as

$$\begin{aligned}
\pi^Y \left(\frac{n_k^X + 1}{\mathcal{N}}, \frac{m_k}{\mathcal{N}} \right) - \pi^Y \left(\frac{n_k^X}{\mathcal{N}}, \frac{m_k}{\mathcal{N}} \right) &= \pi^X \left(\frac{n_k^X}{\mathcal{N}}, \frac{m_k + 1}{\mathcal{N}} \right) - \pi^X \left(\frac{n_k^X}{\mathcal{N}}, \frac{m_k}{\mathcal{N}} \right) \\
\pi^Y \left(\frac{n_j^X - 1}{\mathcal{N}}, \frac{m_j}{\mathcal{N}} \right) - \pi^Y \left(\frac{n_j^X}{\mathcal{N}}, \frac{m_j}{\mathcal{N}} \right) &= \pi^X \left(\frac{n_j^X - 1}{\mathcal{N}}, \frac{m_j}{\mathcal{N}} \right) - \pi^X \left(\frac{n_j^X - 1}{\mathcal{N}}, \frac{m_j + 1}{\mathcal{N}} \right).
\end{aligned}$$

Evaluating the sums, we find

$$\begin{aligned}
2(L(D_{k|j}^X \underline{\phi}) - L(\underline{\phi})) &= \pi^X \left(\frac{n_k^X}{\mathcal{N}}, \frac{n_k^Y}{\mathcal{N}} \right) + \pi^X \left(\frac{n_k^X}{\mathcal{N}}, 0 \right) - \pi^X \left(\frac{n_j^X - 1}{\mathcal{N}}, \frac{n_j^Y}{\mathcal{N}} \right) - \pi^X \left(\frac{n_j^X - 1}{\mathcal{N}}, 0 \right) \\
&+ \pi^X \left(\frac{n_k^X}{\mathcal{N}}, \frac{n_k^Y}{\mathcal{N}} \right) - \pi^X \left(\frac{n_k^X}{\mathcal{N}}, 0 \right) + \pi^X \left(\frac{n_j^X - 1}{\mathcal{N}}, 0 \right) - \pi^X \left(\frac{n_j^X - 1}{\mathcal{N}}, \frac{n_j^Y}{\mathcal{N}} \right).
\end{aligned} \tag{68}$$

Finally, combining terms and canceling others, we arrive at our desired result

$$L(D_{k|j}^X \underline{\phi}) - L(\underline{\phi}) = \pi^X(\vec{\phi}_k) - \pi^X(\vec{\phi}_j - \delta\phi\hat{e}^X). \tag{69}$$

2. Relaxational dynamics

Given the existence of the utility potential function $F[\vec{\phi}(x)]$, one can define a dynamics for $\phi^a(x, t)$ such that $F[\vec{\phi}(x)]$ plays the role of a Lyapunov function ensuring the relaxation of the system toward a stationary state, as done for physical systems [127]. One important difference is that the utility potential function will be *maximized*, as contrasted with a physical free energy which is minimized.

As the microscopic dynamics consist solely of particles moving, the macroscopic dynamics must conserve the total particle number,

$$\partial_t \phi^a(x, t) = -\partial_x J^a(x, t). \tag{70}$$

where $\partial_x = \partial/\partial x$. Analogously to physical system, we take the particle current $J^a(x, t)$ to obey the constitutive relation

$$J^a(x, t) = +M^{ab}(\vec{\phi}) \partial_x \frac{\delta F}{\delta \phi^b}. \tag{71}$$

$M^{ab}(\vec{\phi})$ is a density dependent mobility matrix, which we take to be given by

$$M^{ab}(\vec{\phi}) = \delta^{ab} \phi^b \psi. \tag{72}$$

Recalling $\psi = 1 - \sum_c \phi^c$, this form enforces that both empty ($\phi^b = 0$) and full ($\psi = 0$) locations give zero-flux.

$\delta F/\delta \phi^b$ is the functional derivative of the potential $F[\vec{\phi}(x)]$ that plays the role of a chemical potential [160]. Eq. (71) says that the particle current flows *up* spatial gradients of the chemical potential. We now evaluate the chemical potential as

$$\frac{\delta F}{\delta \phi^b} = -T \left(\ln \phi^b - \ln \psi \right) + (1 - \alpha) \frac{\partial \ell}{\partial \phi^b} + \alpha \frac{\partial u}{\partial \phi^b} + \Gamma \partial_x^2 \phi^b. \tag{73}$$

Taking the gradient, we obtain

$$\partial_x \frac{\delta F}{\delta \phi^b} = -T \frac{\psi \partial_x \phi^b + \phi^b \partial_x \psi}{\psi^b \psi} + (1 - \alpha) \partial_x \frac{\partial \ell}{\partial \phi^b} + \alpha \partial_x \frac{\partial u}{\partial \phi^b} + \Gamma \partial_x \partial_x^2 \phi^b. \quad (74)$$

Finally multiplying by the mobility matrix $M^{ab} = \delta^{ab} \phi^b \psi$, we get our general form for relaxational sociohydrodynamics

$$\partial_t \phi^a(x, t) = T \left((1 - \phi^b) \partial_x^2 \phi^a + \phi^a \partial_x^2 \phi^b \right) - \partial_x \left(\phi^a \psi \partial_x \left[(1 - \alpha) \frac{\partial \ell}{\partial \phi^a} + \alpha \frac{\partial u}{\partial \phi^a} + \Gamma^a \partial_x^2 \phi^a \right] \right). \quad (75)$$

In the special case where the compatibility condition Eq. 64 holds, the derivative of the link function $\ell(\vec{\phi}(x))$ is given by (here, we take $b = X$. The calculation for $b = Y$ proceeds analogously)

$$\begin{aligned} \frac{\partial \ell}{\partial \phi^X} &= \frac{1}{2} \left(\pi^X(\phi^X, \phi^Y) + \pi^X(\phi^X, 0) + \int_0^{\phi^Y} d\psi \frac{\partial \pi^Y(\phi^X, \psi)}{\partial \phi^X} \right) \\ &= \frac{1}{2} \left(\pi^X(\phi^X, \phi^Y) + \pi^X(\phi^X, 0) + \int_0^{\phi^Y} d\psi \frac{\partial \pi^X(\phi^X, \psi)}{\partial \psi} \right) \\ &= \frac{1}{2} \left(\pi^X(\phi^X, \phi^Y) + \pi^X(\phi^X, 0) + \pi^X(\phi^X, \phi^Y) - \pi^X(\phi^X, 0) \right) \\ \frac{\partial \ell}{\partial \phi^X} &= \pi^X(\phi^X, \phi^Y). \end{aligned} \quad (76)$$

where we used the compatibility condition Eq. (64) to go from the first to the second line. In this case, Eq. (75) becomes

$$\partial_t \phi^a(x, t) = T \left((1 - \phi^b) \partial_x^2 \phi^a + \phi^a \partial_x^2 \phi^b \right) - \partial_x \left(\mu^a(\vec{\phi}) \left[(1 - \alpha) \partial_x \pi^a + \partial_x \frac{\partial u}{\partial \phi^a} + \Gamma^a \partial_x \partial_x^2 \phi^a \right] \right). \quad (77)$$

where $b \neq a$. This is the same equation as Eq. 54, showing that our coarse-grained equations are equivalent to the relaxational dynamics when the compatibility condition holds.

H. Linear Stability Analysis

We now attempt to make predictions about the onset of patterns and their subsequent dynamics using linear stability analysis. We consider perturbing around a spatially uniform state densities, $\vec{\phi}(x, t) = \vec{\phi}_0 + \delta \vec{\phi}(x, t)$, where the components ϕ_0^a satisfy $\phi_0^a > 0$ and $\sum_c \phi_0^c \leq 1$. Writing the perturbation as a plane wave, $\delta \vec{\phi}(x, t) = e^{st - iqx} \delta \vec{\phi}_0$, where $s = \sigma + i\omega$ is a complex number describing the growth rate σ and oscillation frequency ω of the perturbation with wavenumber q , our equations of motion reduce to the eigenvalue problem

$$s \delta \phi_0^a = J^{ab}(\vec{\phi}_0) \delta \phi_0^b \quad (78)$$

with the Jacobian matrix with elements

$$J^{ab}(\vec{\phi}_0) = q^2 D^{ab}(\vec{\phi}_0) - q^4 \Gamma \delta^{ab} \mu^b(\vec{\phi}_0), \quad (79)$$

where δ^{ab} are elements of the identity matrix. Given that $\mu^a(\vec{\phi}) = \phi^a(1 - \phi^X - \phi^Y)$ and we are restricted to $\phi^X + \phi^Y \leq 1$, the q^4 term acts to stabilize patterns at large wavenumber q (short wavelength) if $\Gamma > 0$, which we will always take to be true. The eigenvalues of J^{ab} , given by s , determine the stability of the homogeneous state.

If we restrict ourselves to the condition where $\phi_0^X = \phi_0^Y = \phi_0$, then $\mu^X = \mu^Y = \phi_0(1 - 2\phi_0)$ and the eigenvalues are given by

$$s = q^2 \lambda_D(\vec{\phi}_0) - q^4 \Gamma \phi_0(1 - 2\phi_0). \quad (80)$$

where $\lambda_D(\vec{\phi}_0)$ are the eigenvalues of the matrix with elements $D^{ab}(\vec{\phi}_0)$. The growth rate and oscillation frequencies are given by

$$\sigma = \text{Re}(s) = q^2 \text{Re}(\lambda_D) - q^4 \Gamma \phi_0(1 - 2\phi_0) \quad (81a)$$

$$\omega = \text{Im}(s) = q^2 \text{Im}(\lambda_D). \quad (81b)$$

The system's stability is entirely determined by the eigenvalues of the diffusion matrix D^{ab} . The system is stable if all $\text{Re}(\lambda_D) < 0$, while the system is unstable if at least one $\text{Re}(\lambda_D) > 0$. In the case with two species, these eigenvalues take the usual form for 2×2 matrices,

$$\lambda_D^\pm = \frac{D^{XX} + D^{YY}}{2} \pm \sqrt{\left(\frac{D^{XX} - D^{YY}}{2}\right)^2 - D^{XY}D^{YX}}. \quad (82)$$

I. Linear utilities

Here, we will specialize to the particularly simple class of utilities that are linear in the densities. Specifically, we will consider

$$\pi^X(\vec{\phi}) = \kappa^{XX}\phi^X + \kappa^{XY}\phi^Y \quad (83a)$$

$$\pi^Y(\vec{\phi}) = \kappa^{YX}\phi^X + \kappa^{YY}\phi^Y. \quad (83b)$$

In all of the following, we set $\kappa^{XX} = \kappa^{YY} = 1$, thus measuring the utilities in units of the self-utilities. As described in the methods, we also define $\kappa^\pm = \kappa^{YX} \pm \kappa^{XY}$.

With this choice of utilities, the equations of motion then become

$$\begin{aligned} \partial_t \phi^X &= -\partial_x \left[-T \left((1 - \phi^Y) \partial_x \phi^X + \phi^X \partial_x \phi^Y \right) + \phi^X (1 - \phi^X - \phi^Y) \partial_x \left((1 + \alpha) \phi^X + \gamma_- \phi^Y + \Gamma^X \partial_x^2 \phi^X \right) \right] \\ \partial_t \phi^Y &= -\partial_x \left[-T \left((1 - \phi^X) \partial_x \phi^Y + \phi^Y \partial_x \phi^X \right) + \phi^Y (1 - \phi^X - \phi^Y) \partial_x \left(\gamma_+ \phi^X + (1 + \alpha) \phi^Y + \Gamma^Y \partial_x^2 \phi^Y \right) \right], \end{aligned} \quad (84)$$

where we have defined

$$\gamma_\pm = \frac{\kappa^+(1 + \alpha) \pm \kappa^-(1 - \alpha)}{2}. \quad (85)$$

Writing (84) in the form $\partial_t \phi^a = -\partial_x (M^{ab} \partial_x \eta^b)$, we get

$$\begin{aligned} \partial_t \phi^X &= -\partial_x \left[\phi^X (1 - \phi^X - \phi^Y) \partial_x \left(-T(\ln(\phi^X) - \ln(1 - \phi^X - \phi^Y)) + (1 + \alpha) \phi^X + \gamma_- \phi^Y + \Gamma^X \partial_x^2 \phi^X \right) \right] \\ \partial_t \phi^Y &= -\partial_x \left[\phi^Y (1 - \phi^X - \phi^Y) \partial_x \left(-T(\ln(\phi^Y) - \ln(1 - \phi^X - \phi^Y)) + \gamma_+ \phi^X + (1 + \alpha) \phi^Y + \Gamma^Y \partial_x^2 \phi^Y \right) \right]. \end{aligned} \quad (86)$$

From (86), we extract the diffusion matrix as

$$\mathbb{D}(\vec{\phi}) = -T \begin{pmatrix} 1 - \phi^Y & \phi^X \\ \phi^Y & 1 - \phi^X \end{pmatrix} + (1 - \phi^X - \phi^Y) \begin{pmatrix} \phi^X(1 + \alpha) & \phi^X \gamma_- \\ \phi^Y \gamma_+ & \phi^Y(1 + \alpha) \end{pmatrix}. \quad (87)$$

Considering the case of equal densities, $\phi^X = \phi^Y = \phi$ where $0 \leq \phi \leq 0.5$, the diffusion matrix becomes

$$\mathbb{D}(\vec{\phi}) = \begin{pmatrix} D_0 & D_+ - D_- \\ D_+ + D_- & D_0 \end{pmatrix}, \quad (88)$$

where D_0 , D_+ and D_- are given by

$$D_0 = -T(1 - \phi) + \phi(1 - 2\phi)(1 + \alpha) \quad D_+ = -\frac{\phi(2T - \kappa^+(1 + \alpha)(1 - 2\phi))}{2} \quad D_- = \frac{\phi(1 - 2\phi)(1 - \alpha)\kappa^-}{2}. \quad (89)$$

We readily compute the eigenvalues of \mathbb{D} as

$$\lambda_D^\pm = D_0 \pm \sqrt{D_+^2 - D_-^2}, \quad (90)$$

as well as its eigenvectors, which are given by

$$\vec{v}_D^\pm = \begin{pmatrix} \pm \sqrt{D_+^2 - D_-^2} \\ D_+ + D_- \\ 1 \end{pmatrix}. \quad (91)$$

λ_D^\pm become imaginary when

$$|D_-| > |D_+| \Rightarrow |\kappa^-| > \pm \frac{2T - \kappa^+(1 + \alpha)(1 - 2\phi)}{(1 - 2\phi)(1 - \alpha)}. \quad (92)$$

Furthermore, we expect to find pattern formation when $\text{Re}(\lambda_D^\pm) > 0$. This occurs when

$$D_0 \geq \pm \text{Re} \left[D_+^2 - D_-^2 \right]. \quad (93)$$

Fig. 11A shows the amplitude of patterns found, measured using

$$\mathcal{A}[\phi(x)] = \frac{1}{L} \int_0^L dx \sqrt{(\phi(x) - \langle \phi \rangle)^2}. \quad (94)$$

We see that the onset of patterns, given by $\mathcal{A} > 0$, agrees well with the linear stability prediction shown with the white dashed line.

We measure the velocity of the resulting patterns using [155, 191]

$$v = - \frac{\int_0^L dx \partial_t \phi \partial_x \phi}{\int_0^L dx (\partial_x \phi)^2} \quad (95)$$

1. Phase space criteria.

We define the different phases using the following criteria:

- **Segregation:** $\mathcal{S}_H > 0.7$
- **Migration:** $v^a \geq 10^{-9}$
- **Integration:** $\mathcal{S}_H < 0.14$

In order to find regions of coexistence, we perform an annealing procedure, where we change the values of parameters cyclically (Fig. 11D-I). We run simulations for a fixed value of κ_- and a maximal value of κ_+ . After the system has reached a steady state, we decrease κ_+ by a small amount. After reaching a minimum κ_+ , The coexistence region was found by $\mathcal{S}_H^{\text{backward}} - \mathcal{S}_H^{\text{backward}} \geq 0.07$

J. Empirical utility functions

In Fig. 4, we show examples from two other surveys that, in addition to the results shown in Figure 1C of the main text, support the qualitative features of our empirical utility functions – namely that the utility of type A is a monotonically decreasing utility with the proportion of type B, while the utility of type B is peaked for mixed neighborhoods. Further examples of these qualitative results are shown in Fig. 9.

K. Population dynamics

We now consider a microscopic model for growth that is built in the same spirit as agent-based model above. This would lead to a form for S^a which we set to zero in the main text.

We consider individuals within a lattice site can spontaneously die, or reproduce if there is space available in the lattice site, with a rate k dependent on the fitness f^a , $k = k(f^a)$. We denote these processes by the chemical reactions



The reaction rates are given by

$$k(f^a) = \frac{2r}{1 + e^{-\gamma f^a}}, \quad (97)$$

where r is a rate, γ measures the effects of stochasticity in the death/reproduction processes, and the factor of 2 is included for simplicity. Here, we have assumed that both processes have the same r and γ . The form of $k(f^a)$ assures that reproduction (death) occurs more (less) rapidly with increasing fitness.

Assuming mass action kinetics, the density of population a will obey

$$\partial_t \phi^a = \phi^a \left(\phi^\emptyset k(f^a) - k(-f^a) \right), \quad (98)$$

where $\phi^\emptyset = 1 - \sum_b \phi^b$ measures the density of empty sites available to be occupied by reproduction. In the limit of weak selection, $\gamma \rightarrow 0$, we can expand $k(f^a)$ to find

$$\partial_t \phi^a = r \phi^a \left(\gamma f^a - \left(\sum_b \phi^b \right) \left(1 + \frac{\gamma f^a}{2} \right) \right) = S^a. \quad (99)$$